AGU PUBLICATIONS

Geochemistry, Geophysics, Geosystems

RESEARCH ARTICLE
10.1002/2015GC005913

Key Points:
- Tephra, both visible and invisible, can be identified in a rapid, nondestructive manner
- VSWIR spectral parameters can be used to identify tephra and cryptotephra
- The tephrochronologic record of the northern Antilles has been expanded

Correspondence to:
M. C. McCanta,
molly.mccanta@tufts.edu

Citation:
McCanta, M. C., R. G. Hatfield, B. J. Thomson, S. J. Hook, and E. Fisher (2015), Identifying cryptotephra units using correlated rapid, nondestructive methods: VSWIR spectroscopy, X-ray fluorescence, and magnetic susceptibility, *Geochem. Geophys. Geosyst.*, *16*, 4029–4056, doi:10.1002/2015GC005913.

Received 13 MAY 2015
Accepted 10 OCT 2015
Accepted article online 14 OCT 2015
Published online 4 DEC 2015
Corrected 23 DEC 2015

This article was corrected on 23 DEC 2015. See the end of the full text for details.

Identifying cryptotephra units using correlated rapid, nondestructive methods: VSWIR spectroscopy, X-ray fluorescence, and magnetic susceptibility

Molly C. McCanta[1], Robert G. Hatfield[2], Bradley J. Thomson[3], Simon J. Hook[4], and Elizabeth Fisher[1]

[1]Department of Earth and Ocean Sciences, Tufts University, Medford, Massachusetts, USA, [2]College of Earth, Ocean, and Atmospheric Science, Oregon State University, Corvallis, Oregon, USA, [3]Center for Remote Sensing, Boston University, Boston, Massachusetts, USA, [4]Jet Propulsion Laboratory, California Institute of Technology, Pasadena, California, USA

Abstract Understanding the frequency, magnitude, and nature of explosive volcanic eruptions is essential for hazard planning and risk mitigation. Terrestrial stratigraphic tephra records can be patchy and incomplete due to subsequent erosion and burial processes. In contrast, the marine sedimentary record commonly preserves a more complete historical record of volcanic activity as individual events are archived within continually accumulating background sediments. While larger tephra layers are often identifiable by changes in sediment color and/or texture, smaller fallout layers may also be present that are not visible to the naked eye. These cryptotephra are commonly more difficult to identify and often require time-consuming and destructive point counting, petrography, and microscopy work. Here we present several rapid, nondestructive, and quantitative core scanning methodologies (magnetic susceptibility, visible to shortwave infrared spectroscopy, and XRF core scanning) which, when combined, can be used to identify the presence of increased volcaniclastic components (interpreted to be cryptotephra) in the sedimentary record. We develop a new spectral parameter (BDI1000VIS) that exploits the absorption of the 1 μm near-infrared band in tephra. Using predetermined mixtures, BDI1000VIS can accurately identify tephra layers in concentrations >15–20%. When applied to the upper ~270 kyr record of IODP core U1396C from the Caribbean Sea, and verified by traditional point counting, 29 potential cryptotephra layers were identified as originating from eruptions of the Lesser Antilles Volcanic Arc. Application of these methods in future coring endeavors can be used to minimize the need for physical disaggregation of valuable drill core material and allow for near-real-time recognition of tephra units, both visible and cryptotephra.

1. Introduction

Explosive volcanic eruptions can disperse large amounts of pyroclastic material (tephra) over a wide geographic range. When preserved subaerially, in ice cores, or in marine and lacustrine sedimentary records, these layers can serve as stratigraphic marker beds that can be used to infer the timing and magnitude of eruptive activity [e.g., *Federman and Carey*, 1980; *Dugmore*, 1989; *Brown et al.*, 1992; *Carter et al.*, 1995; *Eden et al.*, 2001; *Knudsen and Eiríksson*, 2002; *Larsen et al.*, 2002; *Svensson et al.*, 2006], provide independent chronological constraints [e.g., *Kristjánsdóttir et al.*, 2007; *Stoner et al.*, 2007; *Ólafsdóttir et al.*, 2013; *Austin et al.*, 2014], and can be spatially correlated to provide event-coeval tie points [e.g., *Brown et al.*, 1992; *van den Bogaard et al.*, 1994; *Grönvold et al.*, 1995; *Kristjánsdóttir et al.*, 2007]. Assuming conservative tracer properties, sedimentological, petrological, and geochemical analysis of tephra can be used to inform about the timing and source of eruptive events [e.g., *Shane*, 2000; *van den Bogaard and Schmincke*, 2002; *Lowe*, 2011, 2014], identify systematic patterns or variance in terms of eruptive style, eruption magnitude, and repose periods [e.g., *Bonadonna et al.*, 2002; *Larsen and Eiríksson*, 2007; *Le Friant et al.*, 2008], assess the completeness of terrestrial records [e.g., *Carter et al.*, 2004; *Le Friant et al.*, 2008], and examine the nature and evolution of volcanism during the construction of a volcanic complex [e.g., *Larsen*, 2010; *Shane et al.*, 2013]. While subaerially deposited tephra records can be obscured by burial and/or dense vegetation, and may be subject to extensive erosion [e.g., *Le Friant et al.*, 2008; *Shane and Wright*, 2011], evaluation of tephra incorporated into continuously accumulating sediment records can often make for the most complete archive of explosive volcanic events. As sedimentary materials can often be reliably dated (e.g., via ^{14}C, $\delta^{18}O$, U/Th, paleomagnetic secular variation (PSV), or relative (geomagnetic) paleointensity (RPI) data), identification of

tephra layers in sediments has become increasingly important to inform present-day hazard assessment and better constrain the temporal development and evolution of volcanic systems. However, as tephra and sediment composition can vary spatially and temporally, their identification is not always routine, nor straightforward.

Because the geochemical and mineralogical nature of tephra often contrasts with the properties of the background sediment, multiple methods are potentially available to identify, characterize, and document tephra distribution in sediments. Larger tephra deposits (millimeter to meter scale) are often easily visible to the naked eye and can be readily detected and measured by changes in sediment color or texture [e.g., *Turney and Lowe*, 2001; *Lowe*, 2011]. However, the visible tephra record is frequently limited to locations within close proximity to volcanic centers or for very large eruptions that distribute large amounts of material over a wide area (e.g., the 74 ka Toba eruption: *Ninkovich et al*. [1978] and *Matthews et al*. [2012]). Furthermore, if tephra has similar physical characteristics (e.g., texture, color) to the host sediment, they can be difficult to identify using simple sedimentological analyses [e.g., *Cassidy et al*., 2014a].

In addition to the visible tephra record, fine layers of ash can accumulate that may not be readily discernible to the naked eye [e.g., *Houghton et al*., 2000; *Costa et al*., 2012]. Often submillimeter and smaller in scale, these cryptotephra [*Lowe and Hunt*, 2001] can represent smaller eruptions [e.g., *Payne et al*., 2008], and/or eruptions from more distal sources [e.g., *Carey and Sigurdsson*, 1982; *Rose and Chesner*, 1987; *Houghton et al*., 2000; *Costa et al*., 2012], making their identification and characterization important to fully constrain the eruptive history of a volcanic center. Cryptotephra has been identified by a variety of methods, most of which are time-intensive and sample destructive (e.g., sample disaggregation and point counting [*Turney*, 1998; *Blockley et al*., 2005; *Davies et al*., 2007; *Kristjánsdóttir et al*., 2007; *Le Friant et al*., 2008; *Payne et al*., 2008]). Continuous, rapid, and nondestructive scanning techniques are a highly attractive alternative for identifying cryptotephra permitting analysis of greater amounts of material at a higher sampling resolution than traditional techniques. Through exploitation of mineralogical, geochemical, and sedimentological contrasts of tephra with the background sediment, multiple techniques possess strong potential for tephra identification (see *Cassidy et al*. [2014a] for a detailed discussion); however, their integration or optimization has not always been fully explored. Here we combine measurement of magnetic susceptibility, reflectance spectroscopy, and X-ray fluorescence (XRF) core scanning and evaluate their potential for (crypto)tephra identification in Integrated Ocean Drilling Program (IODP) core Site U1396 (Figure 1), which from previous regional studies [e.g., *Le Friant et al*., 2008; *Cassidy et al*., 2014a] is expected to contain an extensive record of visible and subvisible tephra, and cryptotephra.

2. Background on Nondestructive Methods to Identify (Crypto)Tephra From the Lesser Antilles Volcanic Arc

2.1. Lesser Antilles Volcanic Arc

Resulting from the subduction of the Atlantic plate beneath the Caribbean plate, the Lesser Antilles Volcanic Arc hosts a chain of active volcanic islands (Figure 1). Soufrière Hills on the island of Montserrat (active 1995–present) and La Soufrière on the island of Guadeloupe (last eruption 1977) are the most recently active volcanoes in the north-western portion of the Arc; proximity of these two volcanic centers to the core site means that their eruptive record is likely archived in U1396 (Figure 1). During and immediately after an eruptive event, over 90% of fragments erupted from Lesser Antilles volcanoes are transmitted to the ocean [Trofimovs et al., 2006]. Analysis of tephra from the region reveals compositions of glass shards, dense to poorly vesiculated glassy to microcrystalline particles, dark scoria particles, and mineral and lithic fragments [*Le Friant et al*., 2008]. Basaltic and andesitic volcanic fragments include plagioclase, clinopyroxene, orthopyroxene, amphibole, and FeTi oxides [*Harford et al*., 2002] that contrast the dominantly biogenic calcite and aragonite background sediment that accumulates at rates of 2–5 cm kyr^{-1} [*Le Friant et al*., 2013; *Cassidy et al*., 2014a; *Wall-Palmer et al*., 2014].

Close to the island chain, volcanically triggered mass movements (e.g., flank collapse and turbidites) tend to erode and disturb the continuously accumulating sedimentological record [e.g., Trofimovs et al., 2006, 2008, 2013; *Cassidy et al*., 2014b; *Watt et al*., 2012]. More distal sites are less disturbed by mass wasting processes and potentially provide a more complete, near-continuous record of island arc volcanism. However, the inherent trade-off is that these distal sites receive a lower volume of material, potentially making

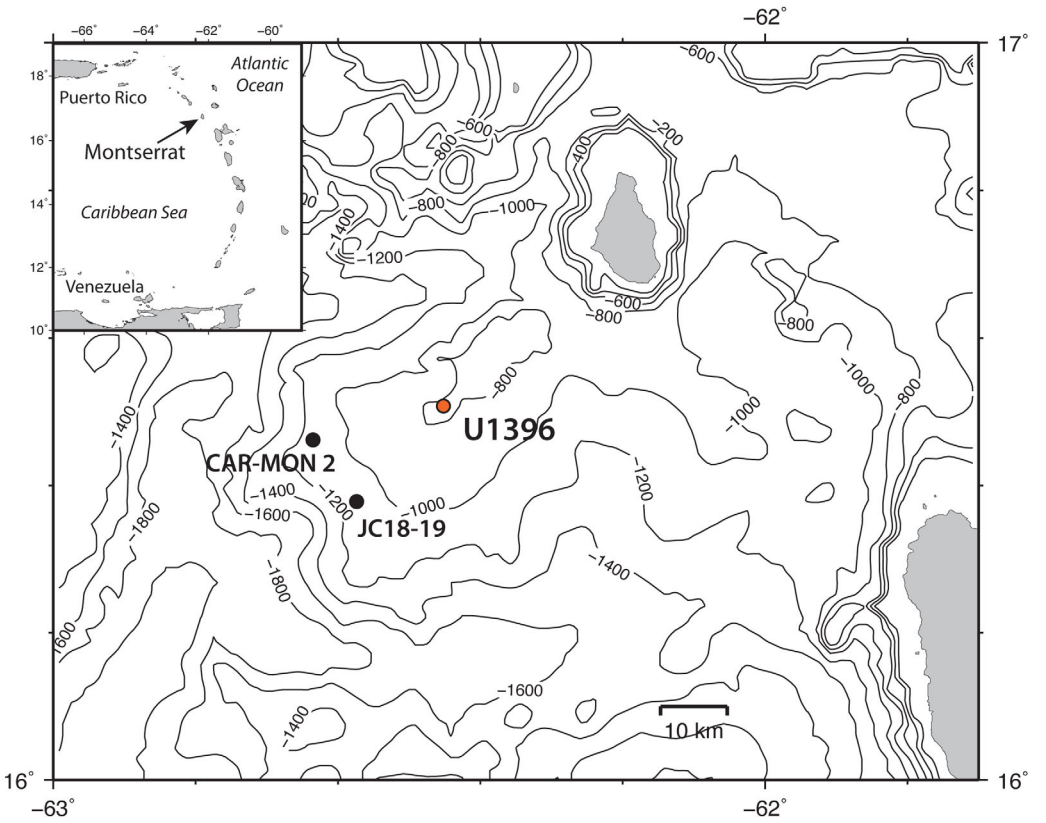

Figure 1. Location of IODP Expedition 340 drill core site U1396 off the coast of Montserrat. The CAR-MON 2 [*Le Friant et al*., 2008] and JC18-19 [*Cassidy et al*., 2014a] sites are identified as well. Bathymetry contour interval is 100 m; data from *Smith and Sandwell* [1997].

identification of tephra more difficult. Two records, JC18-19 (3.6 m, 1130 m water depth, ∼140 ka, Figure 1 [*Cassidy et al*., 2014a]) and CAR-MON2 (5.7 m, 1102 m water depth, ∼250 ka, Figure 1 [*Le Friant et al*., 2008]), collected to the south west of Montserrat contained 15 (JC18-19) and 23 (CAR-MON2) individual layers of volcanic origin over the last ∼250 ka. In JC18-19, 8 of the 15 layers were considered to represent primary fallout while the remaining seven were at least partially reworked volcaniclastic deposits. With strong potential to discriminate tephra from the background autochthonous sediment using the techniques outlined below, these regional records provide additional data with which we can groundtruth our continuous, rapid, and nondestructive data sets.

2.2. Mineral Magnetic Properties

Magnetic measurements are highly sensitive to small changes in the concentration, magnetic grain size, and mineralogy of ferrimagnetic materials [*Thompson et al*., 1975; *Thompson and Oldfield*, 1986; *Dearing*, 1999; *Evans and Heller*, 2003]. Mafic volcaniclastics can possess ferrimagnetic minerals (e.g., magnetite, maghemite, and titanomagnetite) in significant amounts; basalt, for example, can contain up to 10% iron oxides by weight [*Thompson and Oldfield*, 1986] with magnetite phases in concentrations of 1–2% by volume [e.g., *Kristjansson and Jonsson*, 2007]. Andesites, dacites, and other volcanic products can also contain significant proportions of ferrimagnetic phases as secondary minerals [e.g., *Naranjo et al*., 2010], while glass shards can contain micrometer-sized titanomagnetite inclusions [*Ananou et al*., 2003]. In contrast, biogenic silicates and carbonates, which forms the background autochthonous sediment matrix in the Caribbean Sea [*Reid et al*., 1996; *Wall-Palmer et al*., 2012, 2014], possess weak or negative values of magnetic susceptibility (MS) [*Thompson and Oldfield*, 1986; *Polgreen et al*., 1993; *Stoner et al*., 1996; *Pälike et al*., 2010]. Superimposition of ferrimagnetically rich lithic fragments on the carbonate background results in a strong MS response, and as such is frequently exploited to identify the delivery of lithic fragments (e.g., from tephra or ice-rafted debris) to the deep ocean [e.g., *Robinson*, 1986; *Grousset et al*., 1993; *Roberts et al*., 1997; *Stoner and Andrews*, 1999; *Rasmussen et al*., 2003; *Peters et al*., 2010].

While MS can readily detect visible mafic-rich tephra layers, robust and routine identification of cryptotephra has been more problematic [e.g., *Carter and Manighetti*, 2006; *Kristjánsdóttir et al*., 2007; *Gehrels et al*., 2008]. Whole core measurement of MS commonly utilizes a Bartington MS2C loop sensor, often as part of a multisensor track (MST) configuration [e.g., *Gunn and Best*, 1998]. This system integrates MS measurement over several centimeters downcore [*Dearing*, 1999; *Thomas et al*., 2003] meaning that while larger, centimeter-thick tephra deposits are readily identified, signal smoothing inherent to the MS2C system often precludes detection of (sub)millimeter-scale layers. As an alternative, the Bartington MS2E point source sensor integrates MS measurement over 3.8 mm (1.9 mm up and downcore) [*Dearing*, 1999], potentially making it more suitable for detection of small-scale, discrete deposits. Compared to the MS2C, the MS2E is less frequently employed for tephra identification suggesting that significant potential still exists to exploit these magnetic methodologies, particularly when in conjunction with other properties.

2.3. VSWIR Spectroscopy

The reflected visible shortwave infrared (VSWIR) region of the electromagnetic spectrum between 0.4 and 2.5 μm contains strong absorption features due to charge-transfer absorptions in transition metals (dominated by iron) and vibration and overtone bands due to hydroxyl and water (including near 1.4, 1.9, and 2.2–2.5 μm) [e.g., *Farmer*, 1974; *Salisbury et al*., 1991]. The exact position and nature of these bands are specific to the bond strength, length, charge, and coordination state of individual cation-anion pairs, providing a means to identify various carbonate, hydroxyl, iron, phyllosilicate, sulfate, and water-bearing minerals that are often common components in tephra [e.g., *Pieters and Englert*, 1993]. As a result, reflectance spectroscopy has been used extensively and with great success to determine the geochemical composition of terrestrial and extraterrestrial deposits [e.g., *Lucey et al*., 1995; *Bibring et al*., 2006; *Mustard et al*., 2008; *Rivkin and Emery*, 2010].

Although reflectance spectroscopy has not commonly been used to identify pyroclastic deposits in marine cores, several studies have taken advantage of optical spectroscopy due to the nondestructive nature of the measurements. For example, VSWIR spectroscopy was successfully used to identify cryptotephra layers in Irish peats [*Caseldine et al*., 1999] and was used specifically for its rapid, nondestructive analytical nature. Additionally, remote spectroscopic analysis has been used to study the chemistry and physical properties of terrestrial lava and tephra deposits (i.e., shape, grain size, texture, and degree of weathering) [e.g., *Spinetti et al*., 2009; *Hooper and Necsoiu*, 2011; *Tirsch et al*., 2012]. However, for terrestrial analysis, only the visible spectrum has traditionally been utilized resulting in difficulty distinguishing tephra whose minerals are similar in color to those of the surrounding sediments. Extended wavelength range VSWIR spectroscopy provides an opportunity to both discriminate and identify tephras that are invisible to the naked eye but separable at longer wavelengths due to the differing spectral features associated with distinct mineralogies. It is worth noting that measurements at even longer wavelengths in the emitted portion of the electromagnetic spectrum could be used for even greater discrimination and identification as the fundamental vibrational features associated with silicon-oxygen bonding occur around 10 μm in the reststrahlen region. In addition to the analytical features described above, the spatial resolution of the VSWIR spectrometer allows for detection of millimeter-scale features on the order of cryptotephra. The spatial resolution varies due to sample-spectrometer distance; in this study, a contact probe was used resulting in a spot size of ~10 mm.

2.4. Whole Core X-Ray Fluorescence (XRF)

XRF determines sample geochemistry by exploiting the unique wavelengths at which different elements fluoresce when excited by X-rays. Core scanning systems that utilize XRF were developed in the 1990s [*Jansen et al*., 1998] and provide a nondestructive method to obtain sample composition (e.g., Si, K, Ca, Ti, Mn, Fe, Sr, and Zr) in a semiquantitative manner [*Francus et al*., 2009]. Second generation ITRAX scanners have the capability of detecting certain elements at low abundances (e.g., Fe: 25 ppm, Ti: 60 ppm) [*Croudace et al*., 2006] and high spatial resolution (spot size = ~8 mm × 0.5 mm) such that discrete tephra intervals should be readily distinguishable from the carbonate dominated surrounding material.

XRF core scanning has been used to identify tephra in lake cores with some success [*Moreno et al*., 2007; *Langdon et al*., 2011; *Kylander et al*., 2012] though ITRAX can have difficulty in the analytical detection of lighter elements (such as Si) [*Kylander et al*., 2012]. Nevertheless, *Kylander et al*. [2012] were able to identify basaltic tephra layers when shard concentrations exceeded 1000 shards/cm^3 and rhyolitic tephra when concentrations exceeded 850 shards/cm^3. The potential to detect small variations in the geochemical signature

of these deposits makes XRF scanning a very powerful and attractive nondestructive tool to complement the magnetic and spectral properties.

2.5. A Multiproxy Approach

While each of the methods described above are capable of high-resolution measurement, are sample nondestructive, and provide analyses that are relatively rapid and inexpensive to acquire, each have their own analytical weaknesses. MS is only strongly sensitive to the concentration of ferrimagnetic (Fe, Ni, and Co-bearing) phases while the MS2E integrates measurement over several millimeters. XRF measurements can become complicated when grain size differences exist among measured units (which may be a common feature of tephra). Finally, like XRF, VSWIR spectroscopy can only discriminate variations exposed at the split cleaned surface of the sediment core and presently there are no specifically developed VSWIR proxies to understand tephra emplacement.

The purpose of this study is fourfold: (1) to exploit the full capabilities of each measurement technique for cryptotephra identification, i.e., MS measurement using the MS2E, the (sub)millimeter-scale geochemical resolution of the XRF core scanner, and VSWIR spectral measurement; (2) to develop and test a new tephra-specific VSWIR parameter to robustly identify tephra in sediments; (3) to integrate these independent and nondestructive analytical techniques to better assess their viability for cryptotephra identification in marine sediments; (4) to provide an expanded regional tephrochronologic record (~270 ka) for the volcanic island of Montserrat and the northern Antilles arc through measurement of IODP site U1396C and its integration with other regional records from the Caribbean Sea.

3. Methods

3.1. Core Location, Site Setting, and Sampling

Integrated Ocean Drilling Program (IODP) core Site U1396 (16°30.49′N, 62°27.10′W; 801 m water depth; Figure 1) is located in the northern Bouillante-Montserrat half-graben 36 km southwest of the Soufrière Hills volcanic complex on the island of Montserrat and 99 km northwest of La Soufrière on the island of Guadeloupe. Its location on a seafloor topographic high was chosen to minimize the presence of reworked volcanic mass flow units [*Le Friant et al*., 2013]. Site U1396C was cored in 2012 twenty kilometer closer to Montserrat than the shorter CARMON-2 [*Le Friant et al*., 2008] and JC18-19 [*Cassidy et al*., 2014a] records from the region (Figure 1) and therefore potentially contains expanded tephra sequences relative to these records.

For this study, we measured the top 7.5 m of Site U1396C (sections U1396C-1H-1A to U1396C-1H-5A) that the planktic $\delta^{18}O$ record suggests spans the last ~270 ka [*Wall-Palmer et al*., 2014]. Overlap between the upper sections of the U1396C record and the shorter CAR-MON 2 and JC18-19 records of *Le Friant et al*. [2008] and *Cassidy et al*. [2014a] provides an opportunity for existing (crypto)tephra unit correlation and independent verification of the upper U1396C record. Cleaned archive halves of the upper five sections of U1396C (U1396C-1H-1A to U1396C-1H-5A) were sampled using 2 × 2 × 150 cm plastic u-channels in June 2012 that were initially developed for paleomagnetic measurements and are designed to subsample complete sections of core with minimal disturbance. Samples were taken from the more pristine center of the archive half of the core, thus helping to avoid disturbances due to wall/core liner effects. Coring disturbances such as fall-in or flow-in [i.e., *Jutzeler et al*., 2014] were minimal in U1396C making this one of the most pristine records collected during IODP Expedition 340.

3.2. Magnetic Analysis

Measurements of MS were made at 2 mm intervals on the archive half of the split core sections using the Bartington MS2E point sensor on the SHMSL (Section-Half Multi Sensor Logger) onboard the JOIDES (Joint Oceanographic Institutions for Deep Earth Sampling) Resolution during IODP Expedition 340. MS measurements were repeated on the five u-channel samples (with the lid removed and wrapped in plastic wrap) using the MS2E on the GEOTEK XY multisensor logger at the marine geology repository at Oregon State University to test for consistency between the two measurements and to assess any depth shifting that occurred during u-channel sampling. The u-channel was secured in a custom-designed u-channel holder to facilitate and maintain accurate positioning of both the vertical and horizontal axis of the sensor. For comparison with frequently acquired MS2C data and to examine differences in measurement resolution

associated with the MS2E, we repeated MS measurements on the u-channels using the u-channel MS track in the Paleomagnetic and Environmental Magnetic Laboratory (PEML) at Oregon State University. Equipped with a 36 mm diameter MS2C loop under software control using the Bartington MS3 magnetic susceptibility system, measurements were made at 1 cm intervals; the PEML track integrates data over ~3 cm.

3.3. Spectral Analysis

3.3.1. Spectral End-Member Preparation and VSWIR Analysis

To assess the use of spectroscopic methods for identifying (crypto-)tephra, two end-member compositions were measured: volcaniclastic material collected from a terrestrial Montserrat tephra unit collected around 5 km downwind of the Soufrière Hills volcano, and material from a visibly clean layer of marine hemipelagic host sediment in U1396C (U1396C-3H-4A). The volcaniclastic material is andesitic in composition and consists primarily of hornblende and plagioclase crystals, minor FeTi oxides, dense dome rock, and vesiculated material [*Stinton et al*., 2014]; hemipelagic sediment is dominated by calcium carbonate [*Le Friant et al*., 2013]. These samples were dried for 24 h in a 100°C oven, gently disaggregated with an agate mortar and pestle, and sieved using a 200-mesh sieve (74 μm grating). The <74 μm fraction was weighed and mixed in specific proportions to generate 13 samples with different tephra concentrations containing 0, 2, 5, 10, 15, 20, 25, 50, 75, 80, 90, 95, and 100% tephra by weight. Sample mixtures were analyzed at the Brown/NASA RELAB facility using an ASD FieldSpec3® spectrometer between 0.4 and 2.5 μm. A cylindrical aluminum dish was completely filled for each sample, and the sample-filled dish was tapped rather than pressed to minimize preferential orientation of grains. The VSWIR spectra of the five u-channels (with sample caps removed) were acquired every 5 mm under ambient conditions from 0.4 to 2.5 μm using an ASD FieldSpec4® spectrometer at Tufts University.

3.4. XRF and XRD Analysis

U-channels were run through the Cox Analytical Systems ITRAX XRF core scanner at the University of Massachusetts Amherst at a rate of ~1.5 m/d with a sample spacing of 0.5 mm and 10 s count time to collect elemental data (Si, K, Ca, Ti, Mn, Fe, Sr, and Zr).

Clay speciation analysis on a bulk split of visibly clean hemipelagic sediment (sampled from U1396C-3H-4W 70–75 cm depth) was performed by X-ray Diffraction (XRD) at Actlabs (Ontario, Canada). A subsample of the bulk sediment sample was mixed with 10 wt % corundum as an internal standard to determine the amount of poorly crystalline and X-ray amorphous material. Another subsample was dispersed in distilled water and the <25 μm fraction was extracted by wet sieving. Oriented slides of the <25 μm fraction were prepared by placing a sample of the suspension onto a glass slide. In order to detect clay minerals, the oriented slide was analyzed after air drying. XRD analysis was performed on a Panalytical X'Pert Pro diffractometer, equipped with a Cu X-ray source and an X'Celerator detector, operating at the following conditions: 40 kV and 40 mA; range 5°–70° 2θ for the random specimen and 3°–35° 2θ for the oriented specimen; step size 0.017° 2θ; time per step 50.165 s for the random specimen and 50.085 s for the oriented specimen; fixed divergence slit, angle 0.5° for the random specimen and 0.25° for the oriented specimen; sample rotation 1 rps. The quantities of the crystalline mineral phases were determined using the Rietveld method based on the calculation of the full diffraction pattern from crystal structure information. The X'Pert HighScore Plus software along with the PDF-4/Minerals ICDD database were used for mineral identification and quantification.

3.5. Sample Disaggregation and Point Counting Analysis

Preliminary results from MS, VSWIR, and XRF core scanning data were used to identify potential cryptotephra horizons, four of which were subsequently sampled from the working half of U1396C from the IODP Gulf Coast Repository in March 2014. Samples were extracted in 8 cm^3 plastic cubes centered on the potential cryptotephra layer resulting in sediment sampling of 1 cm above and below it within the core. Each cube was then stratigraphically subdivided into four 0.5 cm depth slices for disaggregation and point counting to better constrain the potential cryptotephra location. A sample from the dominantly hemipelagic region submitted for XRD analysis was also disaggregated and point counted to evaluate the background volcaniclastic concentration.

Samples for point counting were treated in 10% HCl for 3 days to disaggregate the carbonate microfossils and then sieved at 40 μm following the method of *Le Friant et al*. [2008] to create a carbonate-free >40 μm

fraction. This fraction was weighed to determine the weight percentage of the >40 μm carbonate free fraction relative to the total weight of the sample.

In each carbonate-free >40 μm fraction, ~400 particles were counted using a binocular microscope to determine the proportion of volcaniclastic material present. Volcanic particles were classified during the counting process using a modified version of *Cassidy et al*. [2014a]. The categories used are as follows: (1) volcanic glass shards and white mineral fragments; (2) black mineral fragments; (3) vesicular or pumiceous material; (4) nonvesicular lava clasts; (5) altered lava clasts (red in color); (6) mafic scoria clasts. The volcanic glass and white mineral fraction was further subdivided into distinct components with an additional count using the petrographic microscope to distinguish between glass and mineral components.

4. Results

4.1. Summary of Routine Shipboard Analyses From IODP Expedition 340

All cores recovered on IODP expeditions are described shipboard for lithology and measured for their magnetic, gamma ray attenuation (GRA: related to density), and visible reflective properties. A summary of these shipboard measurements is given in Figure 2. Three visible volcaniclastic deposits were described in the top 7.5 m of U1396C [*Le Friant et al*., 2013]. Their lithology is described as crystalline and lava rich (concentrations 30–50%) along with bioclastic sand [*Le Friant et al*., 2013]; this is in contrast to the background sediment that is dominated by carbonate ooze and calcareous sand (Figure 2). MS (acquired using a 100 mm MS2C loop) and GRA were measured at 2.5 cm intervals on the unsplit cores on the Whole Round Multi Sensor Logger (WRMSL); L* (sediment reflectivity) was acquired at 5 cm intervals on the split archive half on the Section Half Multi Sensor Logger SHMSL. In general, L* decreases, and density and magnetic susceptibility increase in response to the described visible tephra in the core. However, outside of the visible tephra, the variation in coarsely measured shipboard measured properties appear relatively benign and do not appear sensitive to the 15 volcaniclastic units that were previously described in JC18-19 [Cas*sidy et al*., 2014a] or the 23 volcaniclastic units described in CAR-MON 2 [*Le Friant et al*., 2008].

4.2. XRD Results

Identification of tephra in the region around Montserrat can potentially present a difficult challenge due to the large amount of volcanic material present in the background sediment. Point counting and XRD analysis of hemipelagic sediment indicates that volcanic material comprises ~35% of the average background sedimentary material. This relatively high average volcaniclastic component can result from settling and (re)suspension of volcanic minerals in the water column and/or eolian and hydrologic transport processes. The targeting of a topographic high (Figure 1) during coring of U1396 minimizes the potential for hydrological reworking of materials, e.g., turbidites or submarine mass movements [*Le Friant et al*., 2013], making eolian transport and long duration settling potentially dominant processes to account for the relatively high volcaniclastic background. It is therefore important to recognize that baseline values of MS, reflectance, and XRF core scanning from this region already contain a significant proportion of material of a volcanic nature. However, we also expect intervals related to discrete eruptive events to be in higher concentration than this constant (albeit relatively high) background. XRD analysis of the hemipelagic component is therefore useful to aid better constraining of the spectral mixing model. The minerals identified in the bulk sample and their amounts (wt %) are: calcite (36.4 ± 6.3%), aragonite (3.0 ± 2.8%), plagioclase (25.0 ± 16.1%), illite (2.7%; single analysis), quartz (1.7 ± 0.3%), cristobalite (1.1%; single analysis), and halite (2.1 ± 1.1%). In addition, the bulk sample contains 31.0 ± 13.1% poorly crystalline and X-ray amorphous material (mainly amorphous biogenic silica and volcanic glass). The sediment was found to be highly heterogeneous with respect to the volcaniclastic component (e.g., plagioclase content).

4.3. Magnetic Properties

MS data acquired using the shipboard MS2C and MS2E, the PEML acquired u-channel MS2C, and the Geotek XY acquired u-channel MS2E are shown in Figure 3. U-channel data acquired at the same (in the case of the MS2E) or better (MS2C) sample measurement resolution than those on ship accurately reproduce the trends in the shipboard data; absolute values vary due to the volume differences integrated into each

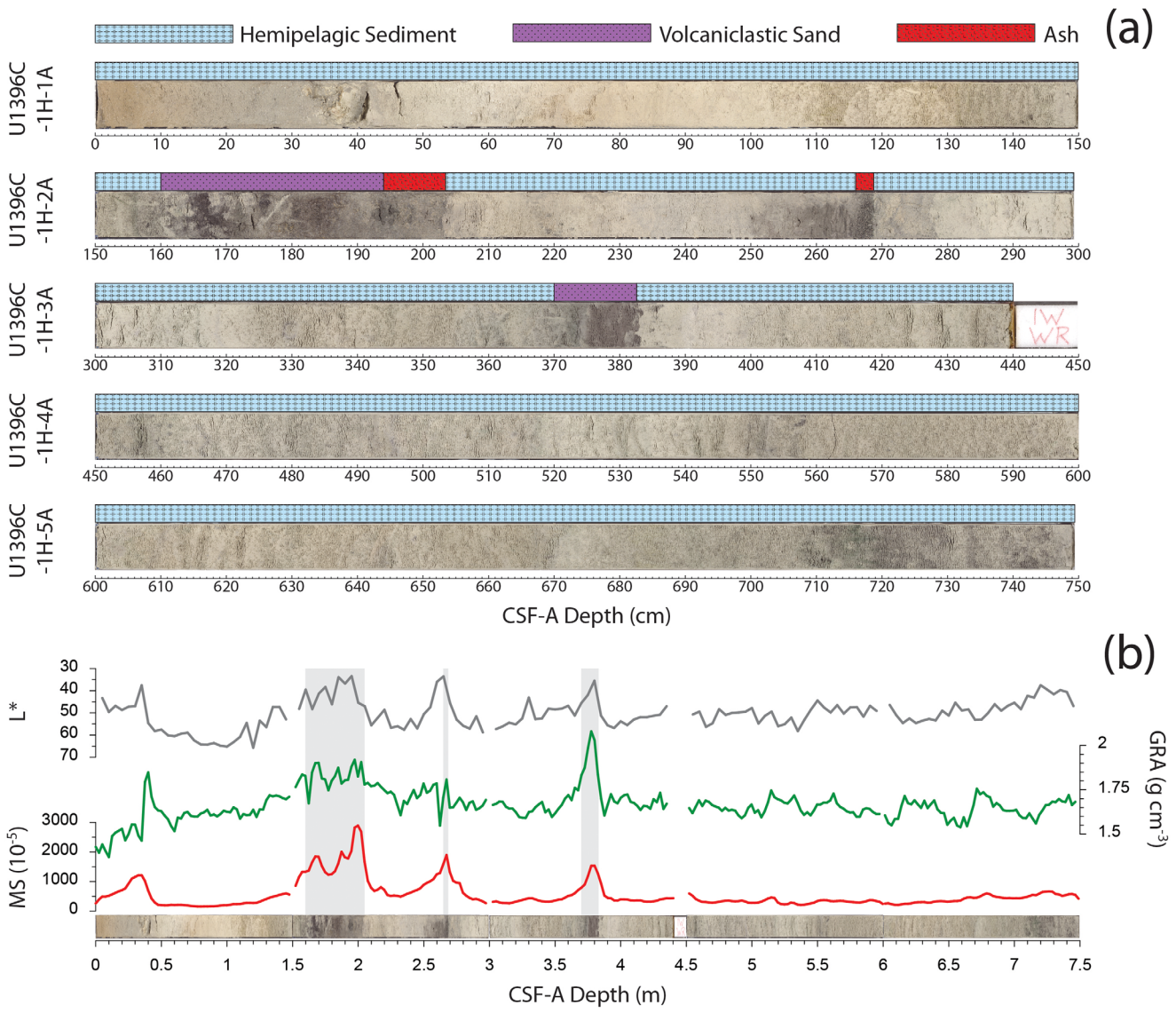

Figure 2. (a) Line scan images and graphic lithology from the visual core descriptions for U1396C-1H-1A to U1396C-1H-5A [*Le Friant et al*., 2013]. (b) Shipboard L*, gamma ray attenuation (as a proxy for sediment density), and magnetic susceptibility. Note how the three shipboard parameters are efficient at discriminating the visible volcaniclastic sand and ash layers (shaded gray regions) from the background calcareous ooze.

measurement. All four measures strongly identify the visible tephra in the core (gray horizontal bars in Figure 3); however, in general, greater structure is revealed in the higher-resolution measurements. For example, while the shipboard MS2C loop data (Figure 3a) clearly identify the visible tephra at 2.7 m with a single peak, u-channel measured MS2C data suggest that three separate peaks might make up the same event (Figure 3b). Higher-resolution u-channel and shipboard MS2E data (Figures 3c and 3d) suggest that the three identified peaks might be discrete individual events as MS returns to almost background values in between peak values.

Comparison of the shipboard U1396C MS2E record to the nearby JC18-19 MS record (Figure 4) [*Cassidy et al*., 2014a] suggests the top ~4 m of U1396C overlaps with the 3.6 m JC18-19 record. Sedimentological analyses, MS, and other proxies in JC18-19 were previously used to identify nine visible volcanic units (VVUs) and six potential cryptotephra in JC18-19 [*Cassidy et al*., 2014a]. Correlation of peaks in JC18-19 MS to peaks in our 2 mm MS2E MS U1396C record suggests all nine VVUs and four of the six potential cryptotephra in JC18-19 can be recognized in the upper 4 m of U1396C **(**Figure 4 and light gray bars in Figure 5**)**. Following a similar approach to *Cassidy et al*. [2014a], we establish a statistical exceedance-based threshold

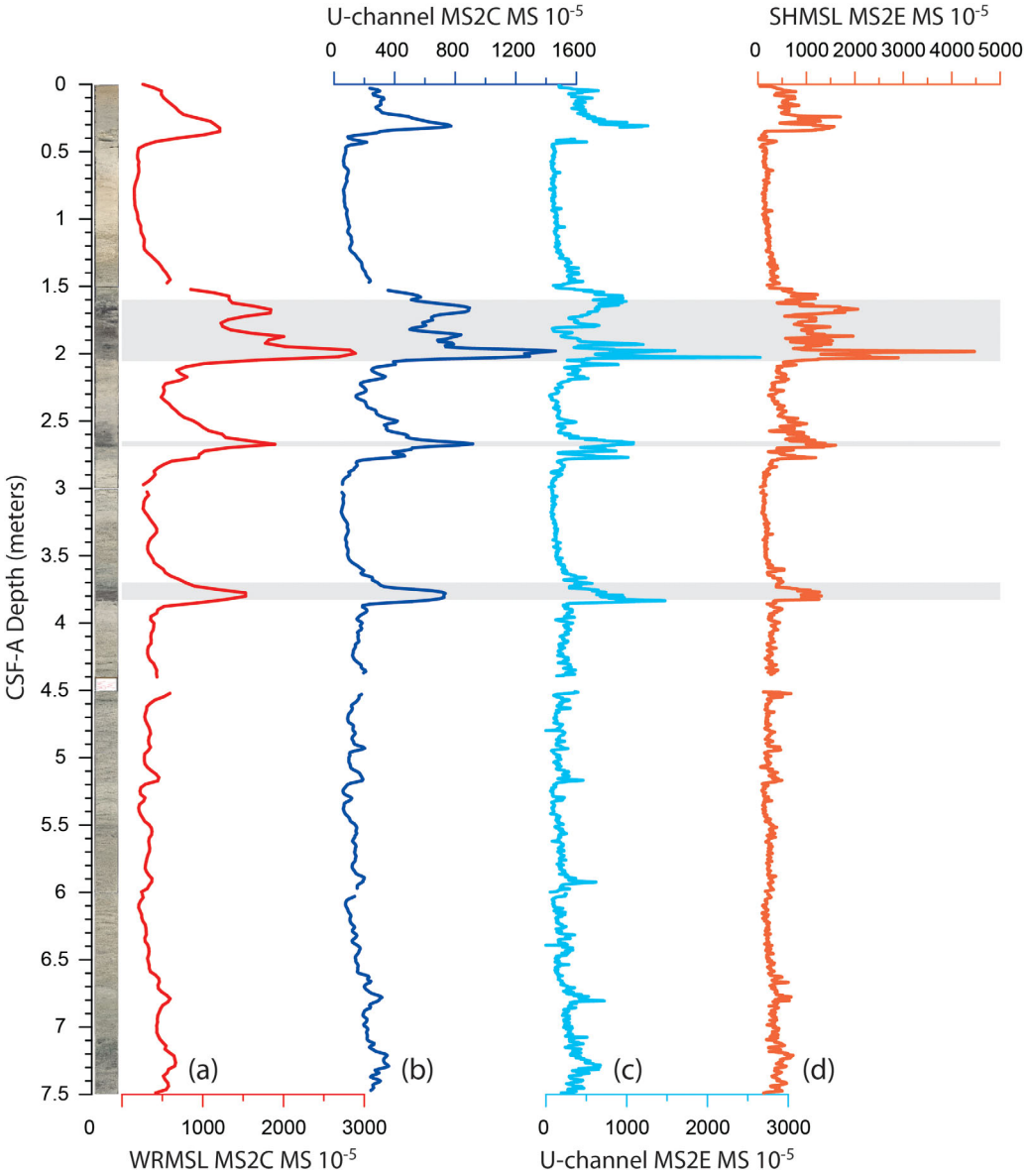

Figure 3. Core images and four measures of magnetic susceptibility, from left to right; shipboard acquired MS2C on the WRMSL at 2.5 cm intervals (red), u-channel MS2C acquired at 1 cm intervals (dark blue), u-channel MS2E acquired at 0.2 cm intervals (light blue), and shipboard MS2E acquired at 0.2 cm intervals (orange). Gray bars mark the location of the visible tephra identified in the visual core description (see Figure 2).

to identify potential cryptotephra in the MS data set. Using intervals of low MS outside of the visible and correlated tephra units (50–120, 300–350, and 470–650 cm), we can define a background average MS value of 194×10^{-5} SI. We use a relatively large interval to calculate the background as this encompasses the natural variability within the core over a relatively long timeframe. We define our threshold as 3 times the standard deviation above the mean (382×10^{-5} SI), exceedance of this value in the data set can be considered statistically anomalous to the background and therefore could potentially contain (crypto)-tephra. The 13 MS peaks that correspond to the 9 VVUs and 4 potential cryptotephra in JC18-19 all exceed this threshold value, accompanied by 4 other MS peaks in the upper 4 m of U1396C (dark gray bars in Figure 5); three of these are under 450×10^{-5} SI (1.36, 1.43, and 1.48 m) and the fourth peaks at 516×10^{-5} SI. With accurate identification of previously identified tephra in JC18-19, we consider this an acceptable threshold for discriminating potential cryptotephra intervals from the hemipelagic background in U1396C.

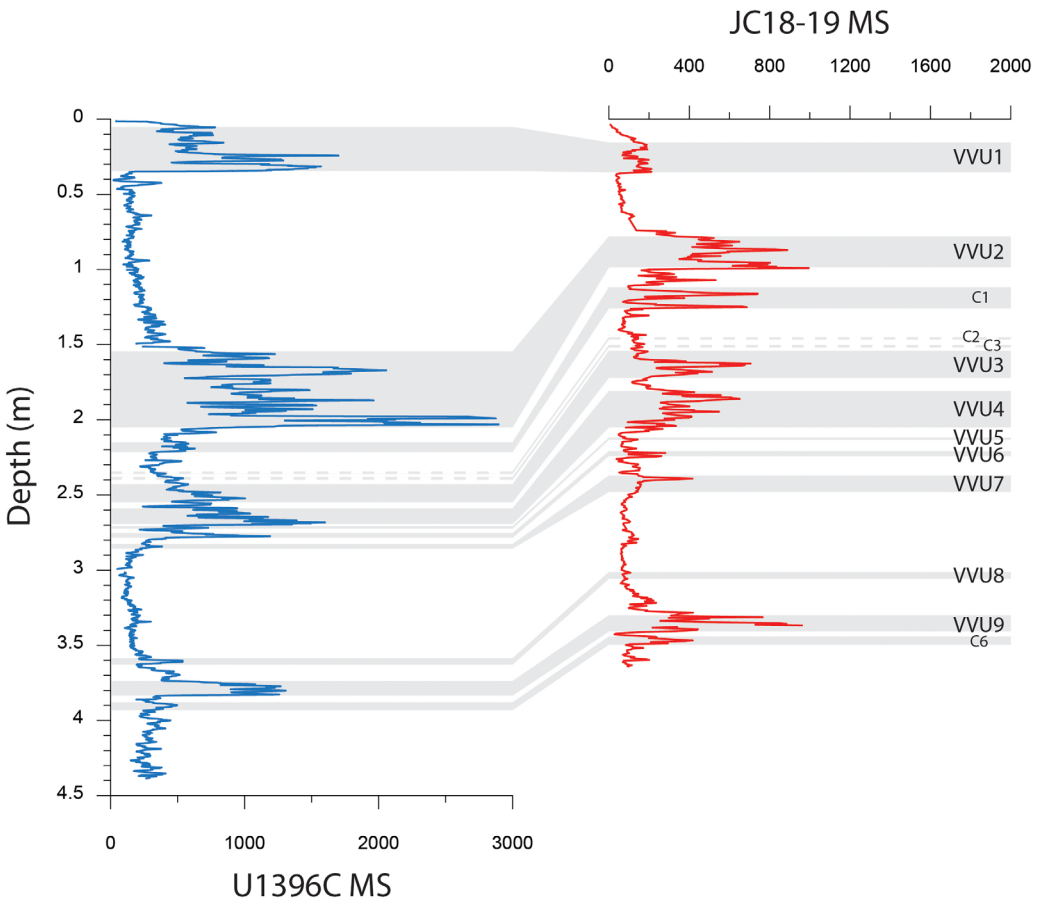

Figure 4. Correlation of shipboard acquired MS2E MS (blue) with MS of nearby core JC18-19 (red) [*Cassidy et al.*, 2014a]. Gray bars denote visible volcanic units (VVUs) in JC18-19 and their coeval layers in U1396C based on correlation of MS; gray dashed bars are used to correlate C2 and C3 as these are not as apparent in the U1396 MS data as other individual events. Slight differences in absolute values between the two cores may result from small volumetric differences integrated into the measurement and or spatial variance.

Below ~4 m, 21 intervals of MS $> 382 \times 10^{-5}$ SI are identified in U1396C (yellow bars in Figure 5); 12 of these are over an 87 cm interval between 6.63 and 7.5 m. The high density of MS exceedances in this interval could reflect a very active period of volcanic activity, or alternatively, higher baseline MS values resulting from a greater concentration of volcanoclastic material in the sediment that fluctuates around the threshold value. To evaluate these alternative hypotheses, we must look to other proxies to help independently identify evidence for discrete tephra and identify any discrete layers that may not produce a strong magnetic response.

4.4. Spectral Properties

4.4.1. Spectral End-Member Mixing Model

Before examining the sediment record of U1396C, we investigated and evaluated the potential to develop a new parameter based on spectral analysis to identify tephra. Collected spectra for the 13 known mixtures of tephra and hemipelagic sediment are given in Figure 6. In these dried samples, there is roughly a factor of 2 variation in overall albedo between the bright hemipelagic sediment (100% sediment) and dark tephra (100% tephra) material. Several key absorption features between 0.4 and 2.5 μm are evident and highlighted with gray vertical bars in Figure 6. In samples with >15% tephra, a notable absorption is present near 1 μm, as well as a broader, shallower absorption near 2 μm. These are likely attributable to ferrous iron (Fe^{2+}) in glass, specifically to spin crystal field transitions of Fe^{2+} in octahedral coordination (consistent with short-range order in glass) [e.g., *Burns*, 1993; *Keppler*, 1992]. A contribution of iron in mafic minerals such as pyroxene (two strong absorption features with minima near 1 and 2 μm) or olivine (broad feature near 1 μm) is also possible [e.g., *Adams*, 1974; *King and Ridley*, 1987; *Cloutis*, 2002]. The exact center position

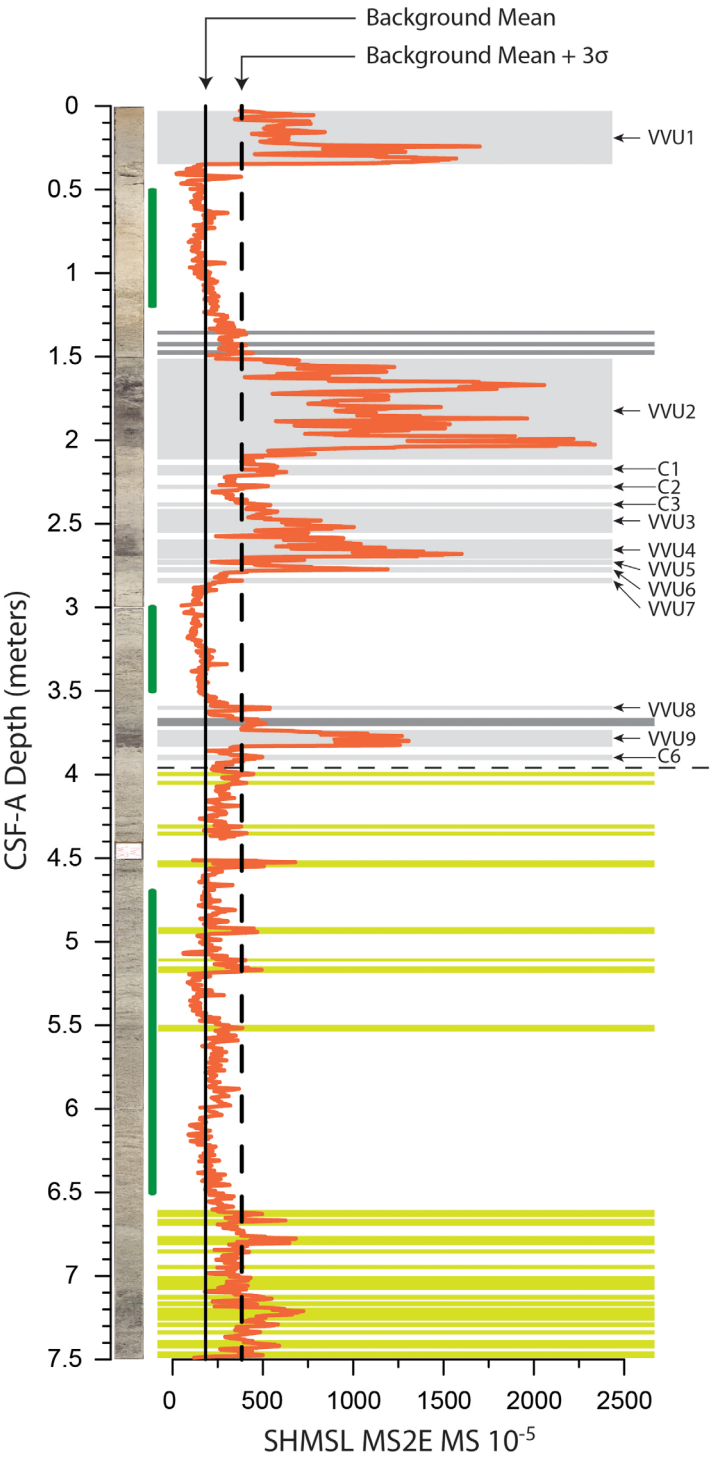

Figure 5. Shipboard acquired MS2E MS alongside the core image for the top five sections of core U1396C-1H. MS values that exceed 3 standard deviations greater than the mean (dashed black vertical line; 382 × 10^{-5} SI) are shaded gray for further investigation. Where U1396C and JC18-19 overlap (above 4.02 m—dashed horizontal black line) this method picks out all nine VVUs and four of the six cryptotephra (C1–C3 and C6) identified in JC18-19 [*Cassidy et al.*, 2014a]. Four cryptotephra are identified from the same interval as JC18-19 that were not correlated with that record (dark gray lines). Green lines indicate additional tephra layers identified below the JC18-19 record.

of the absorption minima near 1 μm varies systematically with mineral composition (e.g., depending on the proportions of Ca, Fe, and Mg in pyroxene or Mg and Fe in olivine), but is generally referred to as the "1 μm feature" even if the band center falls at slightly shorter or longer wavelengths.

In the samples dominated by hemipelagic sediment (sediment concentrations >50%), a pair of absorption features due to metal-OH absorptions in clay minerals are evident at ~2.21 and ~2.35 μm. The strength of these absorption features are roughly (but not exactly) anticorrelated with the strength of the 1 μm feature; as the band depth of 1 μm feature increases, the phyllosilicate or clay mineral features become less apparent. Using these two criteria, the threshold at which tephra is reliably detectable is a concentration of about 50%. A discernable 1 μm feature first becomes evident at a concentration of about 15–20% tephra; the feature is large and unmistakable at a tephra concentration approaching 50%. Fifty percent tephra is also the concentration at which the narrow clay absorption features between 2.2 and 2.3 μm become muted and difficult to detect.

Other spectral features evident include the ~1.4 μm overtone band (O-H stretch) and ~1.9 μm combination overtone (H_2O symmetric and asymmetric stretches; indicated with dashed vertical lines in Figure 6). While it is tempting to consider these overtone bands of water and hydroxyl as indicators of the presence of hydrated phyllosilicate minerals in these laboratory samples, this approach is infeasible in the natural core samples. Core samples

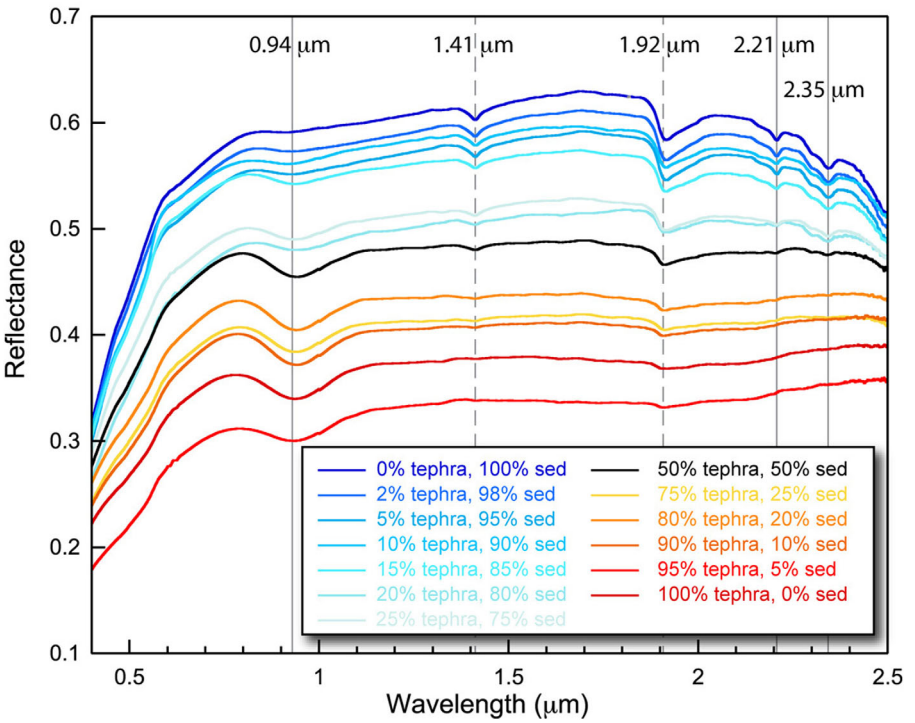

Figure 6. Visible to shortwave infrared spectra of binary mixtures of tephra and hemipelagic sediment. Key absorption features used to distinguish tephra from sediment are highlighted with gray vertical lines; vertical dashed lines indicate H_2O symmetric and asymmetric stretches not considered in the proposed identification method.

were not dried prior to analysis and thus contain variable amounts of surface and adsorbed water in addition to water bound in the interlayer region of clay minerals, making these features indistinguishable and therefore unreliable mineralogical indicators for our purpose [*Hook et al*., 1999; *Baldridge et al*., 2009; *Hecker et al*., 2011].

4.4.2. Development of New Tephra Specific Spectral Summary Parameters

Exploiting the results of the two-component mixture spectra described above, we devised three spectral summary parameters [e.g., *Murchie et al*., 2000; *Pelkey et al*., 2007] to rapidly assess the large number of spectra collected along a core. BDI1000VIS was developed to capture the integrated band depth near the 1 μm region, and BD2p2 and BD2p35 were created to detect absorption features in clay minerals at 2.2 and 2.35 μm, respectively.

To calculate BDI1000VIS, we first find the reflectance maximum between 0.442 and 0.992 μm. This is accomplished by fitting a ninth-order polynomial to the spectrum in this region, evaluating the polynomial at each wavelength point, and finding the maximum value (R_{max}). This reflectance maxima is used to normalize the reflectance values between 0.883 and 1.023 μm, and the BDI1000VIS parameter is then calculated by computing the sum of 1.0 min the normalized reflectance values (equation (1)):

$$\mathrm{BDI1000VIS} = \sum 1 - R_i / R_{max}. \tag{1}$$

Here R_i is the reflectance value at the *i*th wavelength between 0.883 and 1.023 μm.

The 2.2 and 2.35 μm absorption band depth (BD) parameters (BD2p2 and BD2p35) are determined according to equation (2).

$$\mathrm{BD} = 1 - R_C / R_{C*}, \tag{2}$$

where R_C is the reflectance at the center of the spectral band and R_{C*} is the modeled reflectance at the center of the band (defined in equations (3)–(5) and illustrated in Figure 7).

$$R_{c*} = \mathrm{a}R_S + \mathrm{b}R_L \tag{3}$$

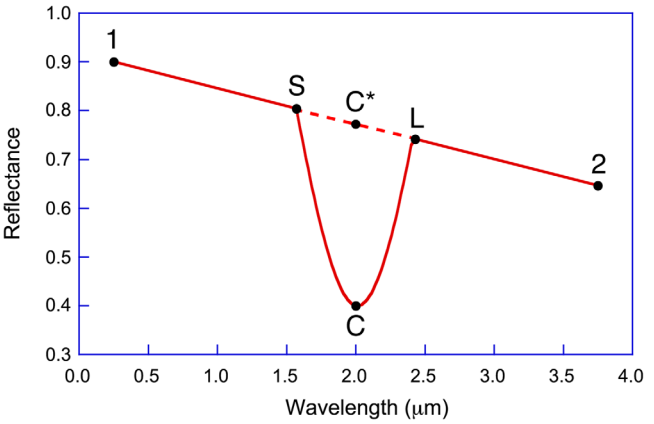

Figure 7. Idealized spectrum indicating absorption band depth parameter calculation. The band depth is defined as $1 - R_C/R_{C*}$, where the point *C* is the center of the given absorption band, R_C is the reflectance at that wavelength, and R_{C*} is a linear fit to the continuum between the short wavelength λ_S and long wavelength λ_L sides of the absorption band [from *Pelkey et al.*, 2007].

$$a = b - 1 \quad (4)$$

$$b = (\lambda_C - \lambda_S)/(\lambda_L - \lambda_S) \quad (5)$$

R_{C*} is therefore a linear fit between the long wavelength (λ_L) and short wavelength (λ_S) areas outside the designated band.

4.4.3. VSWIR Spectral Results

Spectral data for the upper 7.5 m of U1396C were collected and evaluated using the spectral summary parameters discussed above with the resulting variations in BDI1000VIS and BD2p2 presented in Figure 8. Strong increases in BDI1000VIS are observed in the visible tephra units, indicative of a more Fe-rich mineralogy than found in the hemipelagic sediment. Corresponding decreases in the parameters related to clay mineralogy, BD2p2 and BD2p35 (not plotted), are also observed in the visible tephra units resulting from decreased clay content in the hemipelagic sediment due to the increased volcaniclastic volume. When attempting to identify regions of interest for cryptotephra, neither BD2p2 nor BD2p35 were found to be particularly sensitive to the introduction of a volumetrically small cryptotephra layer. For this reason, we consider BDI1000VIS to be the better spectral parameter for potentially detecting cryptotephra.

For the VSWIR background, we chose a core region that shows minimal spectral variation to define a background type section (322–332 cm) and again following the approach of *Cassidy et al.* [2014a] we calculated a threshold value three standard deviations above the mean to identify intervals statistically considered anomalous and therefore potentially containing higher concentrations of (crypto)tephra (BDI1000VIS = above 0.0007; BD2p2 = below 0.0033). Using this metric, 29 regions were identified for further investigation based on variations in the BDI1000-VIS parameter over the 7.5 m record of U1396C (Figure 8) in addition to the three visible units already observed.

4.5. XRF Core Scanning Results

Due to the primary andesitic and mafic mineralogy of the volcaniclastic materials in this region [e.g., *Harford et al.*, 2002], Fe and Mn potentially serve as useful discriminants of tephra composition. The elemental concentrations of Fe and Mn can be normalized for their Ca concentration (ln(Fe/Ca) and ln(Mn/Ca)) to provide an estimate of the mafic to intermediate volcaniclastic composition relative to the background carbonate dominated sediment [*Cassidy et al.*, 2014a] (Figure 9). The natural log of these values was used to diminish differences at large positive compositional values, but to also amplify differences in the compositional data at values between 0 and 1 where the majority of the XRF data falls. The XRF core scanning data are quite noisy, likely due to grain size variations in these mixed samples which at the coarser sedimentary tail approach the measurement resolution of 500 μm (Figure 9). To reduce the noise, a 15-point moving average was applied to smooth the data over 7 mm (3.5 mm up and down core). Using the same background interval as the spectral data (322–332 cm), we statistically generated 3σ threshold values for ln(Fe/Ca) and ln(Mn/Ca) of −0.88 and −4.91 (black lines in Figures 9c and 9d). Comparison to the JC18-19 record [*Cassidy et al.*, 2014a] shows that ln(Fe/Ca) values in U1396 exceed the 3σ threshold value (gray areas in Figures 9c and 9d**)** for all eight corresponding VVUs in JC18-19 (XRF of VVU1 was not measured in JC18-19); ln(Mn/Ca) fares slightly less well, only failing to identify the small unit corresponding to VVU7 in JC18-19 [*Cassidy et al.*, 2014a]. Below 4 m and outside of the overlapping regions of U1396 and JC18-19, 22 additional regions in ln(Fe/Ca) and 16 regions in ln(Mn/Ca) were identified in U1396C for further investigation (Figure 9).

5. Discussion

5.1. Combining Parameters to Identify Cryptotephra in U1396C

5.1.1. Comparison of the Parameters Used to Identify Cryptotephra

All five parameters (MS, BDI1000VIS, BD2p2, ln(Fe/Ca), and ln(Mn/Ca)) used to characterize the sediment in U1396C showed strong variation in properties associated with the three visible tephra units in U1396C

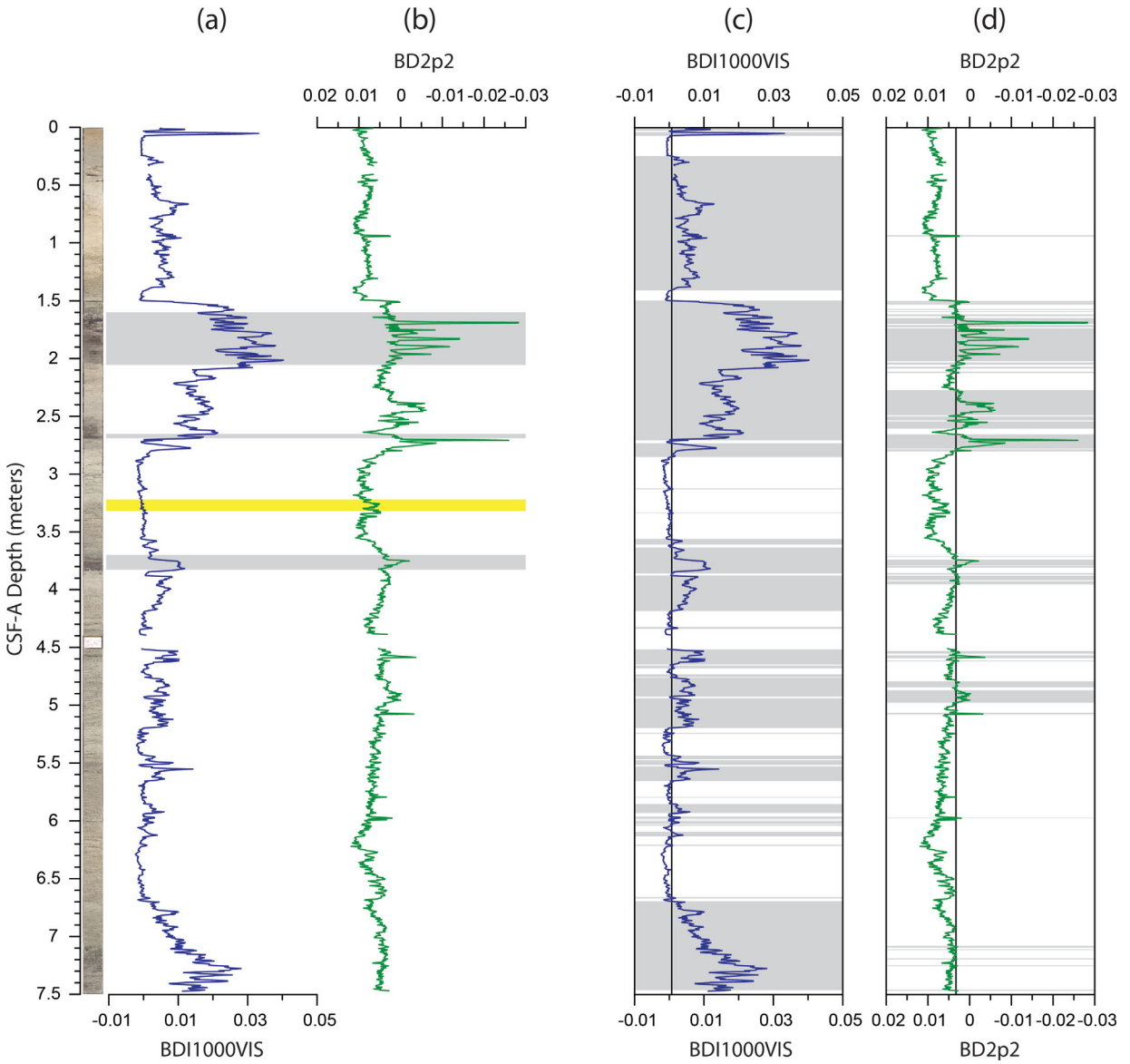

Figure 8. Core image and two of the VSWIR spectral parameters identified to delineate tephra occurrence. (a) BDI1000VIS and (b) BD2p2, both acquired at 0.5 cm intervals. Note that the BD2p2 scale bar is inverted. Gray bars mark the location of the visible tephra identified in the visual core description (see Figure 2). The yellow bar marks the area used for the hemipelagic background. (c) BDI1000VIS and (d) BD2p2 acquired at the same scale as Figures 8a and 8b. VSWIR values that exceed 3 standard deviations greater than the mean (black vertical line; BDI100VIS = above 0.0007; BD2p2 = below 0.0033) are shaded gray for further investigation.

and/or the VVUs and cryptotephra previously identified in JC18-19 by *Cassidy et al*. [2014a]. Interpolation of the MS and XRF core scanning data sets to the same 0.5 cm sampling resolution as the reflectance data set allows direct comparison of different parameters. Correlations between all five parameters are listed in Table 1. The strongest correlation ($r = 0.94$, $n = 1441$) is between the two XRF core scanning data sets (ln(Fe/Ca) and ln(Mn/Ca)) suggesting that iron and manganese minerals cooccur within the sediment and deposited volcaniclastic units in the form of mafic minerals such as FeTi oxides, amphiboles, and pyroxenes. Comparison of the ln(Fe/Ca) XRF core scanning data to the BDI1000VIS reflectance data ($r = 0.66$, $n = 1440$) suggests that the BDI1000VIS data set is sensitive to many of the same Fe-rich layers, likely resulting from the sensitivity of the BDI1000VIS parameter to Fe-absorptions associated with mafic minerals. Relatively strong correlation between MS and BDI1000VIS ($r = 0.66$, $n = 1439$), ln(Fe/Ca) ($r = 0.61$), and ln(Mn/Ca) ($r = 0.63$) further suggests these three parameters are strongly sensitive to Fe-bearing minerals within intermediate to mafic volcaniclastic deposits. In contrast to the XRF core scanning, MS, and BDI1000VIS data, BD2p2 shows a lower correlation to the other parameters with the negatively correlated BDI1000VIS

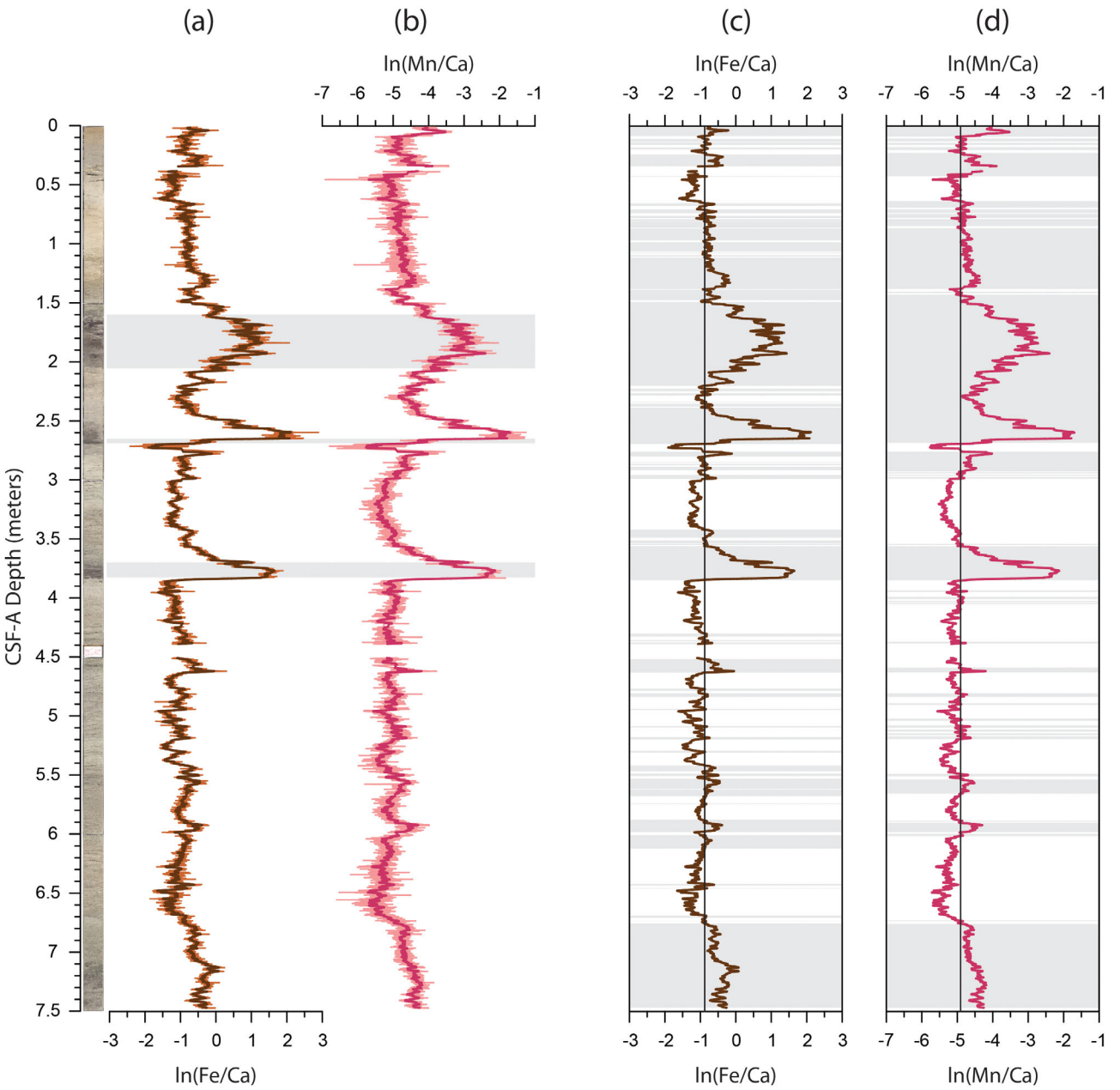

Figure 9. Core image and the XRF core scanning compositional data from U1396C thought to best identify tephra presence. (a) ln(Fe/Ca) and (b) ln(Mn/Ca), both acquired at 0.5 cm intervals. The heavy line in each plot is a 15-point running average used to reduce noise; the actual data are shown in the orange and light pink points, respectively. Gray bars mark the location of the visible tephra identified in the visual core description (see Figure 2). The yellow bar marks the area used for the hemipelagic background. (c) ln(Fe/Ca) and (d) ln(Mn/Ca) acquired at the same scale as Figures 5a and 5b with only the 15-point moving average shown. XRF values that exceed 3 standard deviations greater than the mean (black vertical line; ln(Fe/Ca) = −1, ln(Mn/Ca) = −5) are shaded gray for further investigation.

(r = −0.54) spectral parameter being the strongest relationship. Largely sensitive to the clay mineral content, this negative correlation reflects decreasing clay content with increasing mafic-rich content.

5.1.2. Identification of a Visible Tephra Unit

MS, XRF parameters, and BDI1000VIS appear strongly sensitive to the mafic components within the sediment. However, there is sufficient scatter between different proxies to suggest they are capturing slightly different aspects of the sediment which in combination may be usefully exploited to fully capture the volcaniclastic signature of the sediment. To test the efficacy of each parameter, the spectral properties, MS, and XRF core scanning measurements of a visible tephra layer were first examined (375–383 cm; Figure 10). Threshold values (described in the results section) were exceeded for each of the four parameters

Table 1. Correlation Coefficients of the MS, BDI1000VIS, BD2p2, ln(Fe/Ca), and ln(Mn/Ca) Records[a]

	MS	BDI1000VIS	BD2p2	ln(Fe/Ca)	ln(Mn/Ca)
MS		0.66	−0.44	0.61	0.63
BDI1000VIS	0.66		−0.54	0.66	0.70
BD2p2	−0.44	−0.54		−0.37	−0.41
XRF Fe/Ca	0.61	0.66	−0.37		0.94
XRF Mn/Ca	0.63	0.70	−0.41	0.94	

[a]MS and XRF records were interpolated to the same 0.5 mm measurement resolution as the VSWIR data to facilitate direct comparison. Note the strong correlation between the two XRF data sets which suggests Fe and Mn co-occur in these cores and the generally strong correlation between BDI1000VIS and the MS and XRF data indicating the sensitivity of BDI1000VIS to Fe-bearing phases. Correlations are based on original measured depths and have not been corrected for potential positioning offsets (see section 5.1.3) which would generally act to improve the correlation values.

quantifying the tephra presence. Sharp increases in BDI1000VIS, MS, and XRF core scanning data are observed at the base of the tephra layer (383 cm) and are sustained through the tephra layer (Figure 10). Similarly sharp decreases in BDI1000VIS and MS occur at 375 cm where visible changes in sediment color occur; in contrast, XRF values experience a more gradual decrease going up-core as the tephra layer grades more gradually into the sedimentary background over ~17 cm (Figure 10). A second peak in the XRF core scanning data is also observed at 370 cm that is muted in BDI1000VIS and MS data potentially implying a later event of a composition not resolvable by BDI1000VIS and MS. A concomitant decrease in the parameters related to clay mineralogy BD2p2 and BD2p35 (not plotted) is observed at the base of the visible tephra, increasing only when the tephra unit ends (Figure 10). Together, all three techniques exceed their threshold values indicating a strong response to the large, visible, likely mafic-rich, tephra unit that we can quantify using our developed methodology (Figure 10). Combination and application of these parameters to the 7.5 m U1396C record can therefore be used to identify (crypto-)tephra over the last ~270 ka.

5.1.3. Identification of Potential Cryptotephra

Using exceedances of the thresholds established for each individual parameter, spectral and MS data are used to identify potential cryptotephra in the upper 7.5 m of U1396C. The broader declines observed in the XRF core scanning data make it more difficult to identify the discrete fine-scale nature of cryptotephra so these data are used in a complimentary role alongside the reflectance and MS data sets to support cryptotephra identification. In addition to the 3 visible tephra which produce strong responses (gray bars in Figures 11–15), 29 potential event layers were identified in the upper 7.5 m of U1396 (red bars in Figures 11–15). In each case, exceedance of a minimum of two parameters above the defined threshold indicated departure from the background hemipelagic-dominated sedimentary signature as per the protocol described in *Cassidy et al.* [2014a].

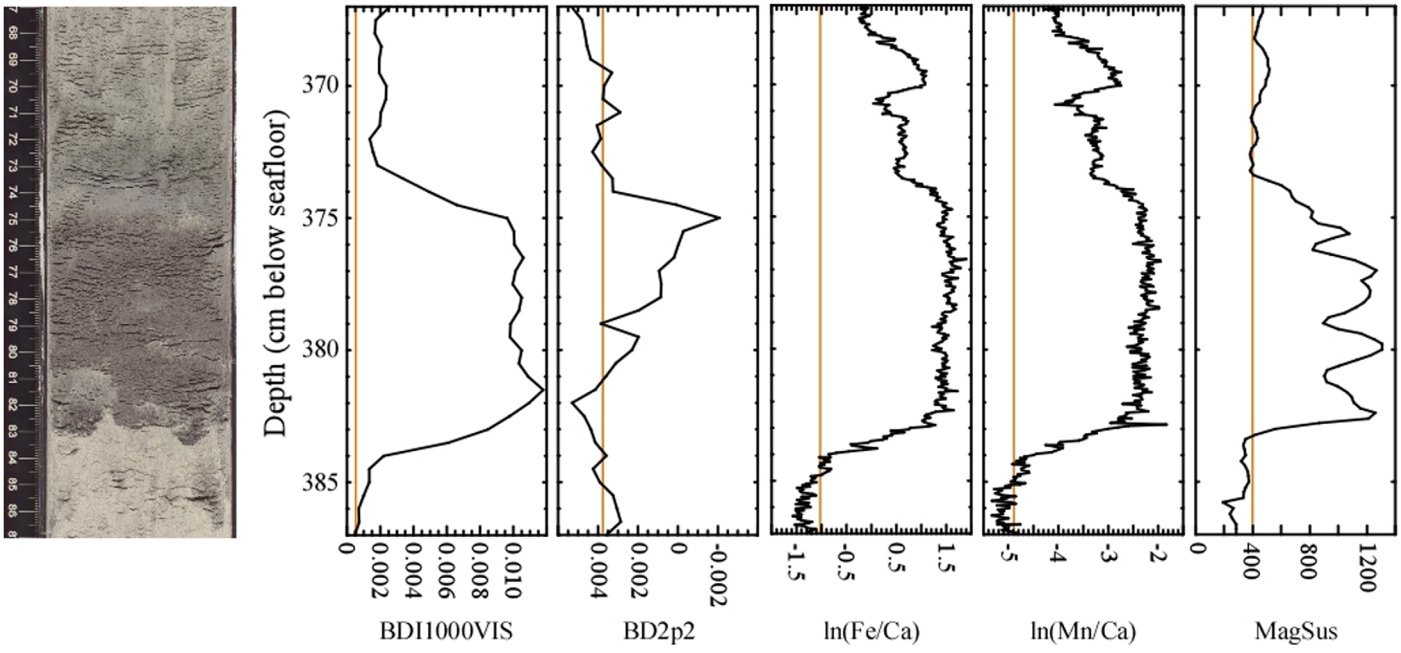

Figure 10. Visible tephra unit in U1396C-1H-3A. The spectral summary parameters BDI1000VIS and BD2p2, magnetic susceptibility, and core scanning XRF geochemical ratios are plotted to show that positive tephra identification is obtained with all techniques for visible units. The vertical orange line represents the 3σ standard deviation above an average background value. Values above this envelope are considered to be distinct from hemipelagic sediment.

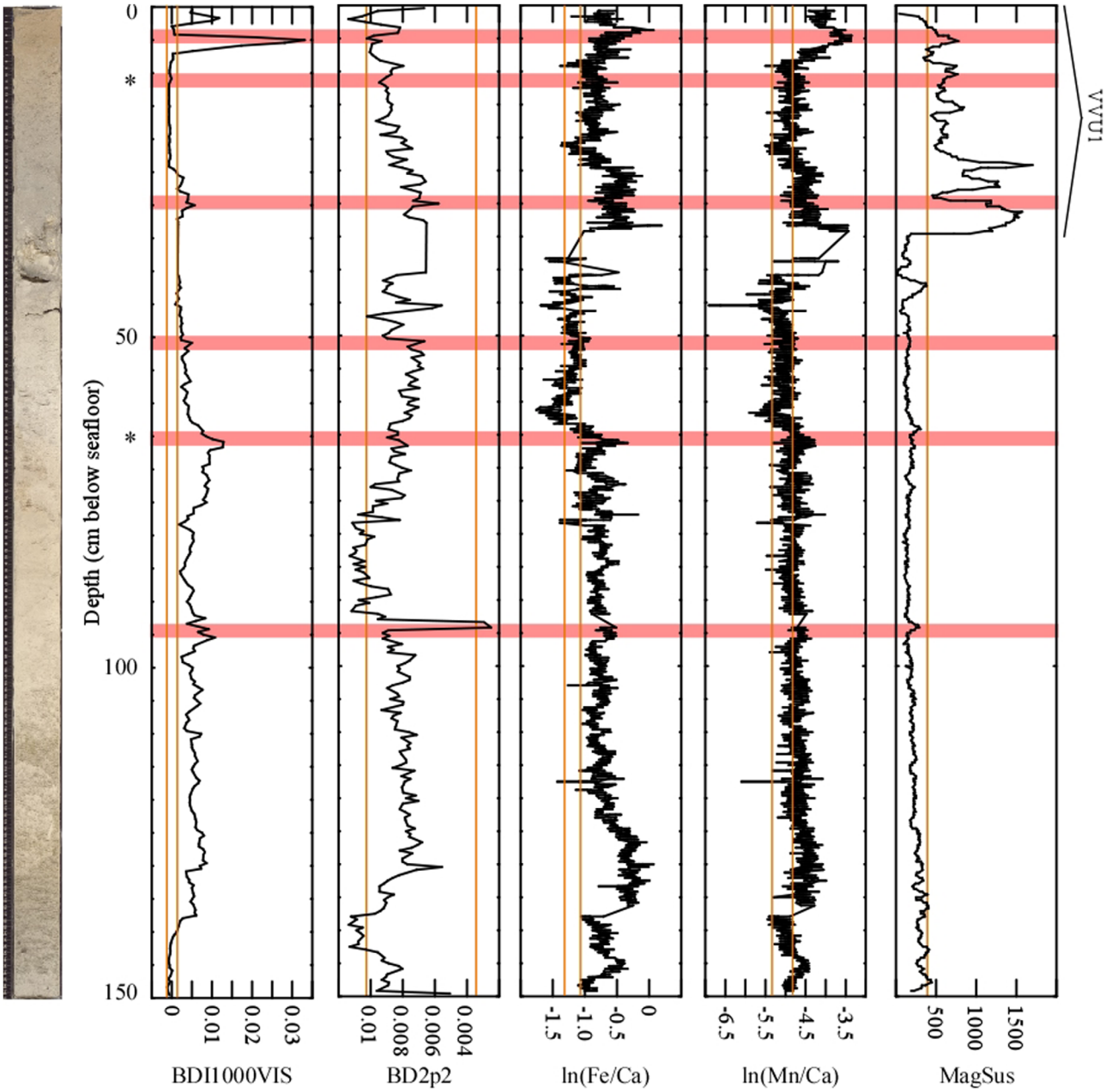

Figure 11. U1386C-1H-1A. The spectral summary parameters BDI1000VIS and BD2p2, magnetic susceptibility, and core scanning XRF geochemical ratios are plotted for comparison. Vertical orange lines represent 3σ standard deviation both above and below an average background value. Values outside of this envelope are considered to be distinct from hemipelagic sediment. Horizontal red shaded boxes indicate depths where two or more parameters indicate the presence of cryptotephra following the approach of *Cassidy et al.* [2014a]. Letters in the right-hand column denote regions of overlap with JC18-19 tephra identification [*Cassidy et al.*, 2014a]. Asterisks indicate locations of point counting.

While the spectral parameter BDI1000VIS and MS were found to best correlate with tephra presence, XRF core scanning results, specifically ln(Fe/Ca), were often positively correlated as well, reinforcing our interpretation (Figures 11–15). The spectral parameters related to the presence of clay species (BD2p2 and BD2p35) were not as useful for reliable cryptotephra identification as the presence of fine-scale cryptotephra does not always significantly affect the clay content of the layer (Figures 11–15). Within the 31 total layers, we discern 11 of the 15 VVU and cryptotephra layers identified by *Cassidy et al.* [2014a] using our combined approach.

Close examination of the independent data sets suggest minor depth offsets may exist as similar peaks in different parameters do not exactly line up (e.g., U1396C-1H-4A layers identified between 550 and 565 cm; Figure 14). Offsets between the shipboard measured MS data and the u-channel measured VSWIR and XRF

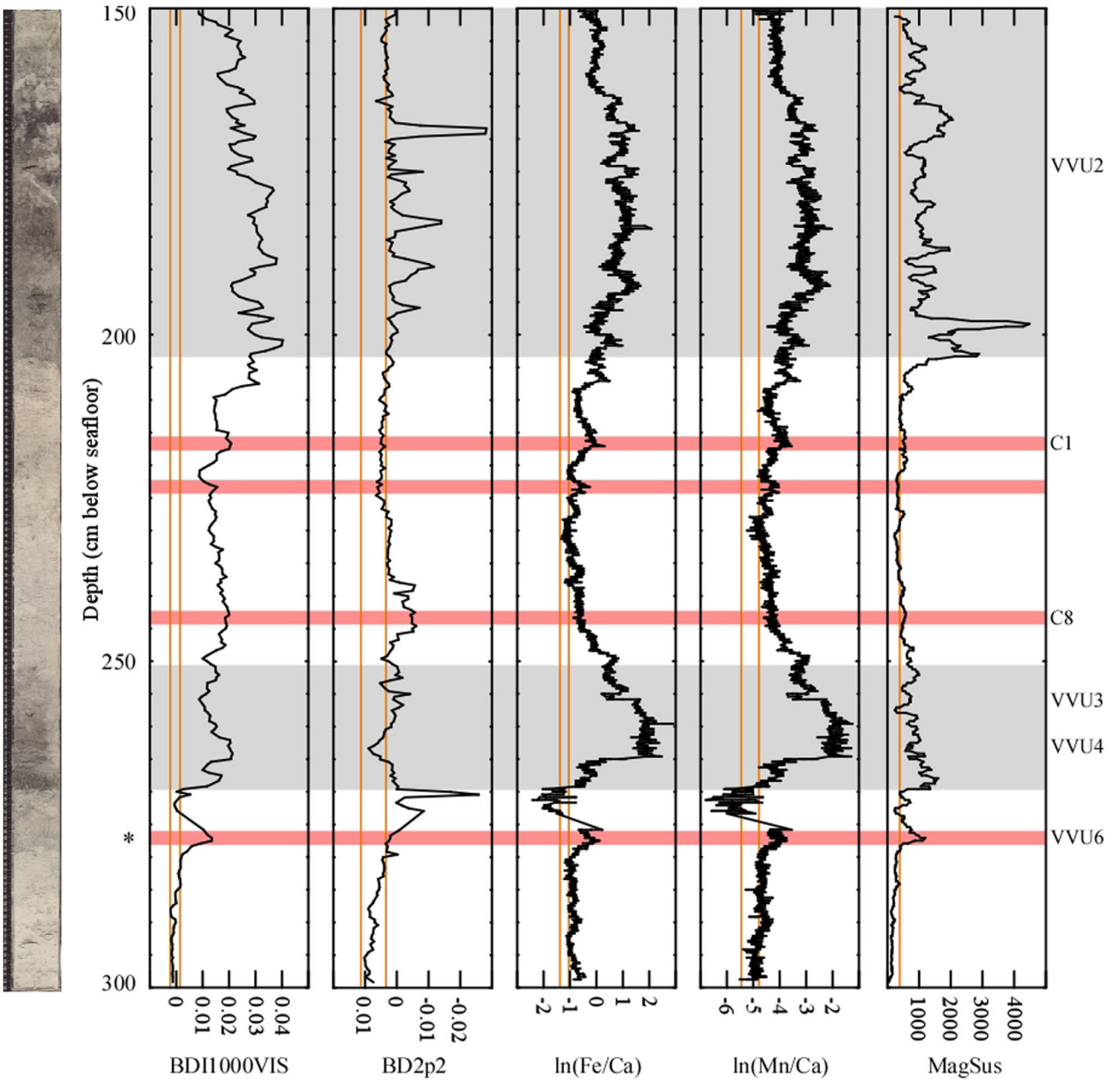

Figure 12. Core U1396C-1H-2A. The spectral summary parameters BDI1000VIS and BD2p2, magnetic susceptibility, and core scanning XRF geochemical ratios are plotted for comparison. The horizontal gray boxes represent the extent of the visible tephra layer. Vertical orange lines represent 3σ standard deviation both above and below an average background value. Values outside of this envelope are considered to be distinct from hemipelagic sediment. Horizontal red shaded boxes indicate depths where two or more parameters indicate the presence of cryptotephra. Letters in the right-hand column denote regions of overlap with JC18-19 tephra identification [*Cassidy et al.*, 2014a]. Asterisks indicate locations of point counting.

core scanning data have two potential origins resulting from positioning errors during u-channel sampling and/or shrinking of the sediment within the u-channel (and potential movement) resulting from unavoidable air drying. The extent of sample translocation can be assessed though comparison of the MS2E data sets measured onboard ship and those measured on the u-channel samples (Figure 3). In general, there is excellent agreement between the two data sets with offsets between prominent features predominantly <1 cm (around the resolution of the VSWIR data). This suggests that significant translocation (>2 cm) may be dominantly related to drying rather than sampling. Only one interval in the lower part of the record exceeds this tolerance. The peak in shipboard MS2E at 7.21 m is shifted 7 cm deeper in the u-channel MS2E data (Figure 3). Reexamination of the u-channel showed significant cracking in this area resulting from drying and explaining the shift and potential offset of the peaks in BDI1000VIS and MS in the lower 50 cm of the record (Figure 15). For

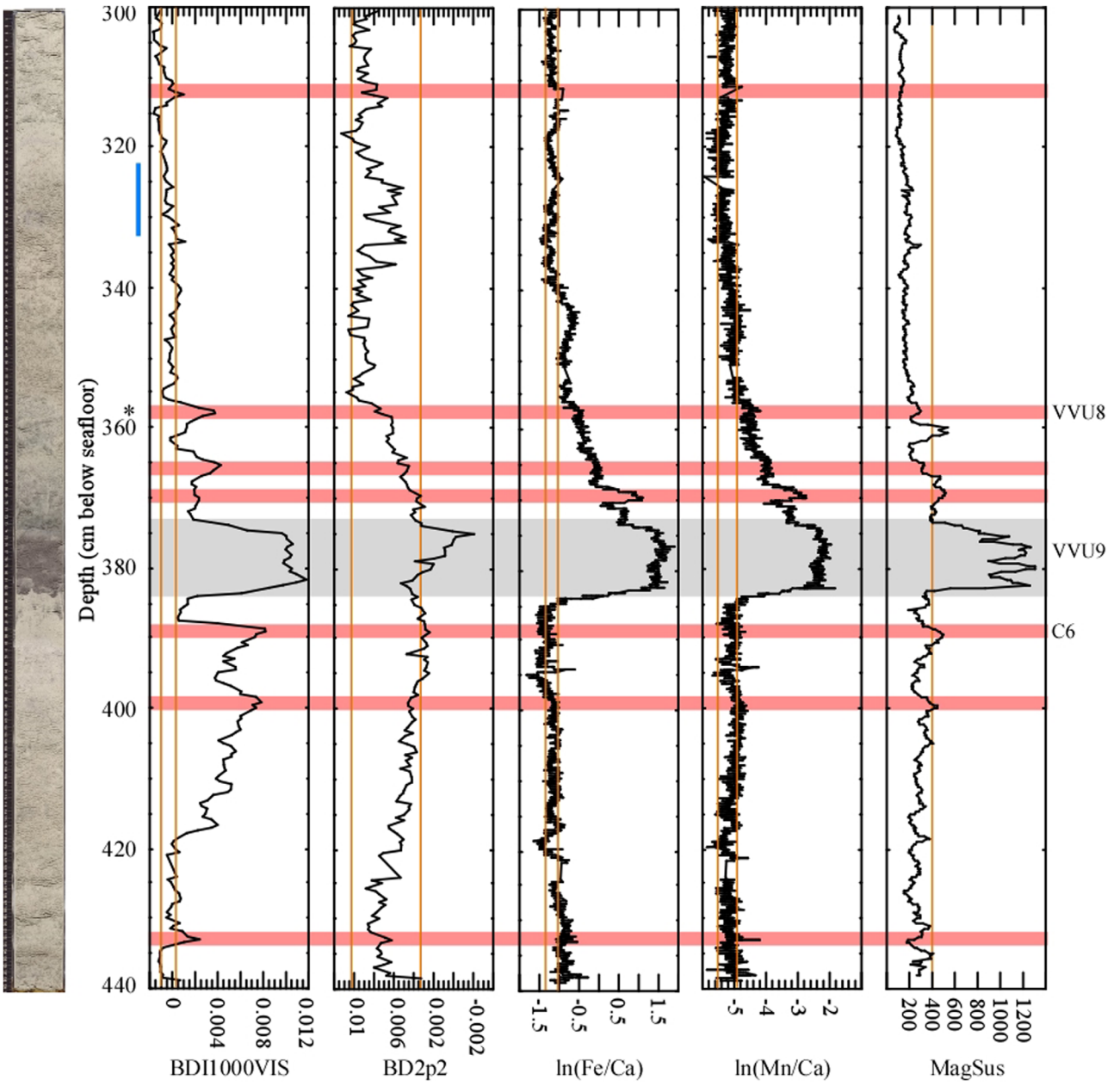

Figure 13. U1396C-1H-3A. The spectral summary parameters BDI1000VIS and BD2p2, magnetic susceptibility, and core scanning XRF geochemical ratios are plotted for comparison. The horizontal gray box represents the extent of the visible tephra layer. Vertical orange lines represent 3σ standard deviation both above and below an average background value (sediment used to represent average background is indicated on the core image by a blue vertical line). Values outside of this envelope are considered to be distinct from hemipelagic sediment. Horizontal red shaded boxes indicate depths where two or more parameters indicate the presence of cryptotephra. Letters in the right-hand column denote regions of overlap with JC18-19 tephra identification [*Cassidy et al.*, 2014a]. Asterisks indicate locations of point counting.

identification of potential cryptotephra, we therefore accept offsets in peak values resulting from positioning errors of ±2 cm.

Several difficulties should be noted. As discussed above, the background volcaniclastic component is high. Therefore, distinguishing additional input from a small eruption can be difficult. In several cases, especially in the lower part of the core, all indicators consistently plot above the threshold established for that data set. (e.g., 495–525 cm and >700 cm; Figures 14 and 15). One likely explanation for this is that these earlier periods (>175 ka) [*Wall-Palmer et al.*, 2014] experienced increased background volcaniclastic fluxes to the core site due to either greater availability and/or transport of material to the core site. Therefore, rather than being discrete eruptive units, although evidence from CAR-MON2 suggests this period experienced

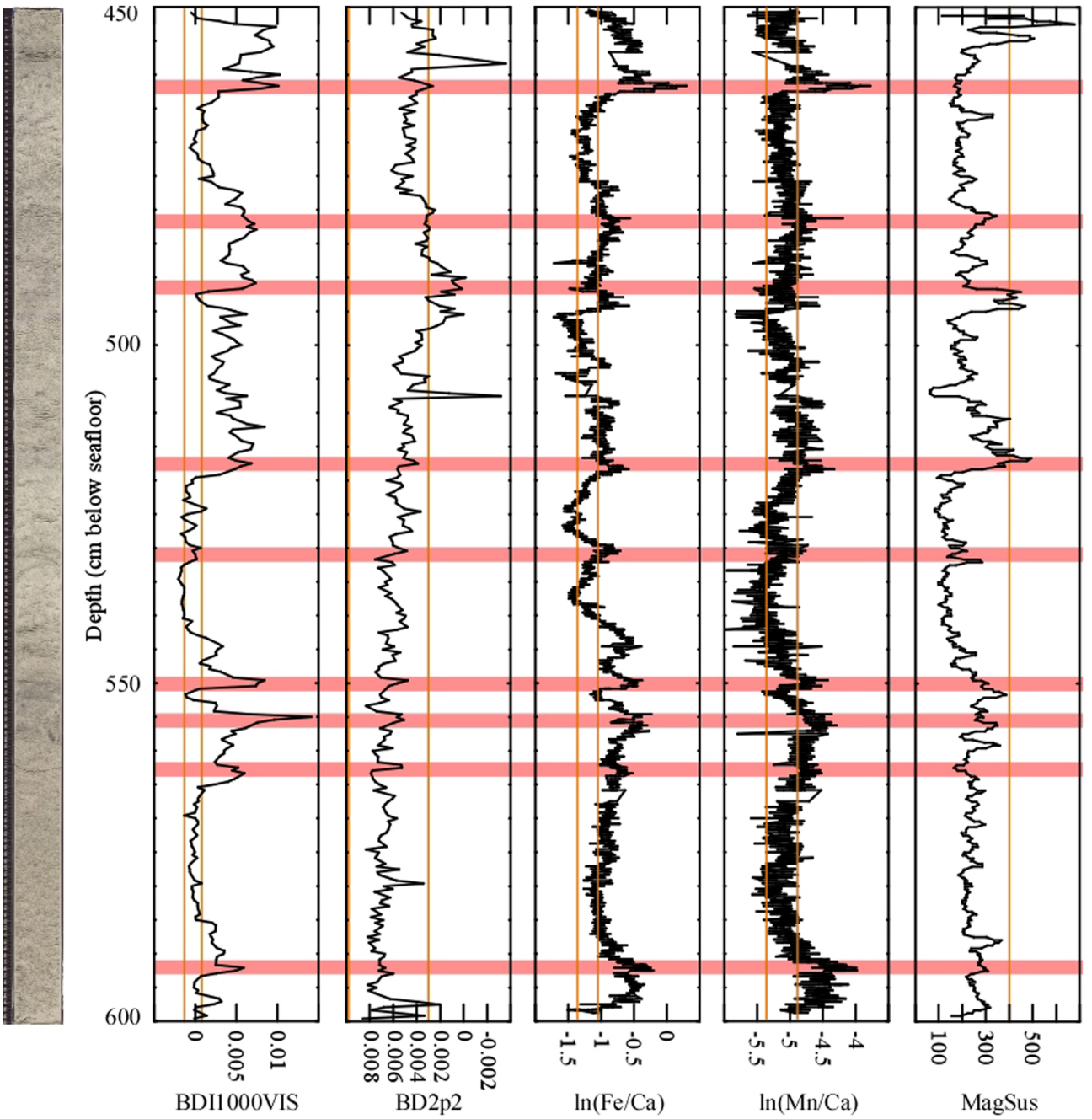

Figure 14. Core U1396C-1H-4A. The spectral summary parameters BDI1000VIS and BD2p2, magnetic susceptibility, and core scanning XRF geochemical ratios are plotted for comparison. Vertical orange lines represent 3σ standard deviation both above and below an average background value. Values outside of this envelope are considered to be distinct from hemipelagic sediment. Horizontal red shaded boxes indicate depths where two or more parameters indicate the presence of cryptotephra.

greater eruptive activity [*Le Friant et al.*, 2008], higher baseline values in all parameters may imply increased volcaniclastic fluxes rather than an increased eruptive frequency. Discrete and well-defined peaks in MS, VSWIR, and XRF core scanning data were used to identify potential cryptotephras within these intervals, however, corroboration of these intervals in this case can only come from more traditional point counting methods.

5.2. Verification of Increased Volcaniclastic Components Through Physical Counting

In order to ascertain if the layers identified above contain increased amounts of volcaniclastic material that could represent a cryptotephra horizon, sample disaggregation and point counting techniques were

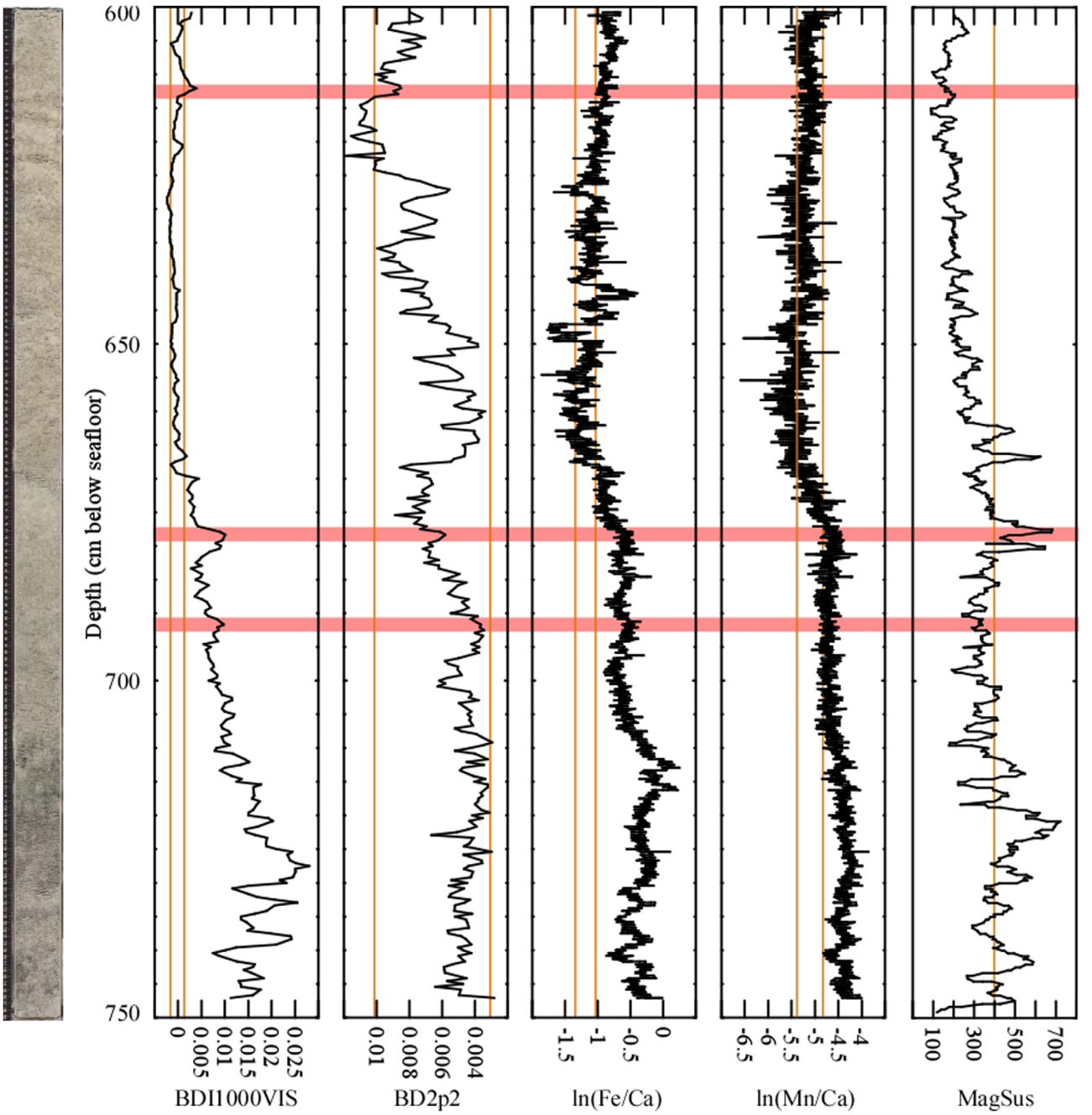

Figure 15. Core U1396C-1H-5A. The spectral summary parameters BDI1000VIS and BD2p2, magnetic susceptibility, and core scanning XRF geochemical ratios are plotted for comparison. Vertical orange lines represent 3σ standard deviation both above and below an average background value. Values outside of this envelope are considered to be distinct from hemipelagic sediment. Horizontal red shaded boxes indicate depths where two or more parameters indicate the presence of cryptotephra.

employed. Here we compare results from the destructive techniques applied in four layers from core sections U1396C-1H-1W, 2W, and 3W (Figures 11–13). Three intervals are characterized by exceedances in multiple cryptotephra indicators (MS, BDI1000VIS, and XRF at 66.5, 277.2, and 357.5 cm depth) while the other interval (11.1 cm depth) shows relatively little response of our cryptotephra proxies, aside from a small increase in BDI1000VIS (Figure 11). Following the definition set forth by *Le Friant et al.* [2008], increase in the glass shard/white mineral fraction was determined to be the best indicator of tephra presence although many other volcanic end-members increased above background levels in potential cryptotephra layers as well (Table 2). The background contained 33.7 glass shards/white mineral fragments per gram of dry sample and therefore presents a useful threshold above which to characterize the presence of cryptotephra.

Table 2. Point Counting Results

			Concentration = Number of Particles Per Gram of Dry Material					
	Depth Below Sea Floor (cm)		White Glass/ Minerals	Black Minerals	Pumice	Nonvescicular Clasts	Altered Lava	Scoria
Background			33.7	1.7	8.4	3.8	0.9	2.8
U1396C-1H-1W	11	11.5	86.8	6.5	52.8	14.0	9.2	5.2
U1396C-1H-1W	11.5	12	65.9	6.1	75.5	14.0	8.7	4.4
U1396C-1H-1W	12	12.5	73.3	9.6	70.7	7.4	9.6	3.9
U1396C-1H-1W	12.5	13	79.0	11.3	49.3	11.8	18.8	4.4
U1396C-1H-1W	66	66.5	122.2	10.9	46.7	13.1	14.0	12.2
U1396C-1H-1W	66.5	67	103.4	9.2	30.5	11.8	13.1	6.5
U1396C-1H-1W	67	67.5	91.2	7.9	27.9	17.9	14.8	12.7
U1396C-1H-1W	67.5	68	120.4	10.0	28.8	20.5	11.3	6.5
U1396C-1H-2W	276	276.5	80.0	19.0	13.0	38.0	17.0	2.0
U1396C-1H-2W	276.5	277	55.1	19.2	10.2	30.4	10.9	1.0
U1396C-1H-2W	277	277.5	95.0	29.8	17.4	51.1	18.0	0.0
U1396C-1H-2W	277.5	278	74.4	27.7	9.9	26.5	11.5	0.8
U1396C-1H-2W	278	278.5	78.1	22.2	8.1	39.7	15.4	1.7
U1396C-1H-2W	278.5	279	77.2	23.7	13.3	31.1	17.0	1.2
U1396C-1H-3W	357	357.5	68.8	6.0	47.7	41.2	13.6	0.0
U1396C-1H-3W	357.5	358	63.8	11.1	43.9	33.8	11.1	1.9
U1396C-1H-3W	358	358.5	78.3	11.3	28.7	55.8	14.8	2.0
U1396C-1H-3W	358.5	359	61.3	8.4	22.1	47.2	18.5	1.8
U1396C-1H-3W	359	359.5	58.8	14.6	20.2	52.7	18.8	2.8

Depth 66.5 cm. VSWIR and XRF indicate strong tephra preference at 66.5 cm (Figure 11); a small MS peak is observed once the data were shifted slightly in relation to the reflectance and XRF core scanning data ($<$1.5 cm) to account for positioning errors (see above discussion). Although peak values are centered between 66 and 66.5 cm, VSWIR and XRF parameters are above threshold values over the whole 2 cm interval sampled for point counting (Table 2 and Figure 11). Point counting revealed that the glass shard/white mineral component is above background levels throughout the interval, averaging 109 shards/g of dry sample. Many other volcaniclastic particles are high in this layer as well including pumice and altered lava clasts (Table 2) providing strong evidence for cryptotephra presence. An increased percentage of black minerals may result in the observed increased MS response.

Depth 277.2 cm. All techniques indicate strong tephra preference at 277.2 cm (Figure 12). Discrete peaks in each of the observed parameters (MS, VSWIR, and XRF) are above threshold levels over the entire 2 cm sampled interval (Figure 12). Point counting reveals the glass shard/white mineral component to be 2–3 times that of the background (Table 2). Both the nonvescicular clasts and altered lava components show order of magnitude increases over the background as well (Table 2**)**. In addition, the black mineral component shows an order of magnitude increase over background and a significant increase over all other point counted layers (Table 2). This results in the 277.2 cm layer having the strongest MS response of any of the point counted layers. Overall, the point counting data indicate an increased amount of volcaniclastic material in the 277.2 cm region consistent with a cryptotephra layer.

Depth 357.5 cm. Reflectance and MS (when shifted $\sim$2.5 cm to account for positioning errors) data both show above threshold values at 357.5 cm (Figure 13). Core scanning XRF indicates that the region is on a slope rising above the identified thresholds, but distinct peaks were not observed above the overall slope. The glass shard/white mineral component is at least 2 times than of the background and order of magnitude increases in pumice, nonvescicular clasts, and altered lava clasts are observed as well (Table 2). Although not as high as in the 277.2 interval, the black mineral concentration shows an order of magnitude increase over the background levels resulting in a strong MS response (Figure 13 and Table 2). As in the previous layers, the point counting data confirm an increased concentration in volcaniclastic material in the region identified by multiple nondestructive methods consistent with a cryptotephra layer.

Depth 11.1 cm. Reflectance, MS, and XRF core scanning data are all at or below their threshold values in this interval which is described as being a bioclastic-rich sand unit containing glass and other lithics [*Wall-Palmer et al*., 2014]; however, a small peak in BDI1000VIS is observed (Figure 11). Point counting over 0.5 cm

intervals from 11 to 13 cm suggests that the glass shard/white mineral concentration is nearly double that of the background in this depth interval (Table 2 and Figure 11) with a significant increase in pumice as well. The lack of either a XRF or MS signal may result from the low concentration of black minerals (although above background) as these phases are likely to be the major carriers of iron in the volcanics. This layer highlights one of the strengths of the multiproxy approach; each method is sensitive to different signals. Therefore, the VSWIR record is not only that of the mafic material (i.e., that recorded by MS and XRF), but also changing in response to the glass shards/white mineral fraction thereby making it very useful in deposits where silicic glass shards are the primary component.

Traditional methods of sample disaggregation and point counting support and validate our hypothesis that the combination of MS and reflectance data (with some corroboration from XRF core scanning results) is capable of identifying regions in which elevated volcaniclastic components may be indicative of cryptotephra. Distinguishing the source of the volcaniclastic material, either primary fallout or reworked mass flow deposits, was not undertaken in this study although the location of U1396C on a topographic high was chosen to minimize the presence of mass flow deposits [*Le Friant et al*., 2013]. Coeval increases in the concentration of glass shards, MS, and reflectance suggest that the nondestructive techniques proposed in this study can successfully identify cryptotephra and can facilitate expansion of the tephrochronologic record of the region to include smaller or more distal eruptions.

5.3. Evaluating Spectral Parameter BDI1000VIS as a Tephra Identification Proxy

Magnetic susceptibility and XRF core scanning techniques have both successfully been applied to identify tephra layers in sediment cores [*Kristjánsdóttir et al*., 2007; *Peters et al*., 2010] and are relatively well-understood proxies. Despite previous attempts at using UV-VIS spectroscopy for tephra characterization [e.g., *Caseldine et al*., 1999], VSWIR methods have not been fully developed for routine identification. Here we developed the spectral parameter BDI1000VIS as a measure of the shape and depth of the 1 μm band [*Pelkey et al*., 2007], which dominantly reflects the concentration of Fe-phases in the system. Strong correlation with the independently generated MS and ln(Fe/Ca) data sets and point counted data strongly supports this interpretation. Therefore, if Fe is present in the volcaniclastic particles that comprise tephra, BDI1000VIS can be strongly sensitive to tephra presence in concentrations as low as 15% at subcentimeter-scale resolution. In contrast, BD2p2 and BD2p35 (as proxies for clay phyllosilicates) only present strong negative correlations with larger visible tephra. In many of the cryptotephra, however, the low abundance of volcaniclastic material means that the majority of the measured sample is hemipelagic sediment. The lack of a negative BD2p2 and BD2p35 correlations with other proxies identifying cryptotephra indicates the lower resolving ability of this spectral parameter for cryptotephra identification.

5.4. Comparison with Previous Studies and Extension of the Tephrochronologic Record of the Northern Antilles Arc

The 5.75 m cryptotephra record of CAR-MON2 (Figure 1) was established through traditional sample disaggregation techniques and point counting every 10 cm, except in visible tephra-rich areas where they were sampled at 5 cm intervals [*Le Friant et al*., 2008]. This methodology identified 20 individual cryptotephra corresponding to 9 dome-forming eruptions and 6 open vent eruptions over the last ~250 kyr [*Le Friant et al*., 2008] (Figure 16). Compared to CAR-MON2, we identified 29 potential cryptotephra in addition to the three visible tephra units (Figure 16). Identification of additional layers may result from the increased sampling resolution of the data set presented in this paper which makes individual measurements at 0.05–0.5 cm resolution opposed to the averaging of point counts over 5–10 cm [*Le Friant et al*., 2008] which precludes identification of multiple cryptotephra within the same sampling interval. Furthermore, the closer proximity of U1396C to Montserrat and Guadeloupe than CAR-MON2 may also result in greater accumulation of tephra in individual event-layers and may also explain the increase in identified layers in U1396C over CAR-MON2. However, as noted above, these units correspond only to regions with increased volcanic content; no distinction is made between primary fallout or reworked material.

One of the overarching goals of IODP Expedition 340 was to expand the tephrochronologic record of the northern Lesser Antilles arc. While event-layers identified in U1396C cannot be exclusively tied to individual eruptive centers without additional geochemical data to discriminate source (e.g., Pb isotopes [*Lindsay et al*., 2005; *Labanieh et al*., 2010; *Cassidy et al*., 2012]), the tephra record can be used to constrain eruptive activity of the northern portion of the arc as a whole. The 3 visible tephra units likely represent the largest

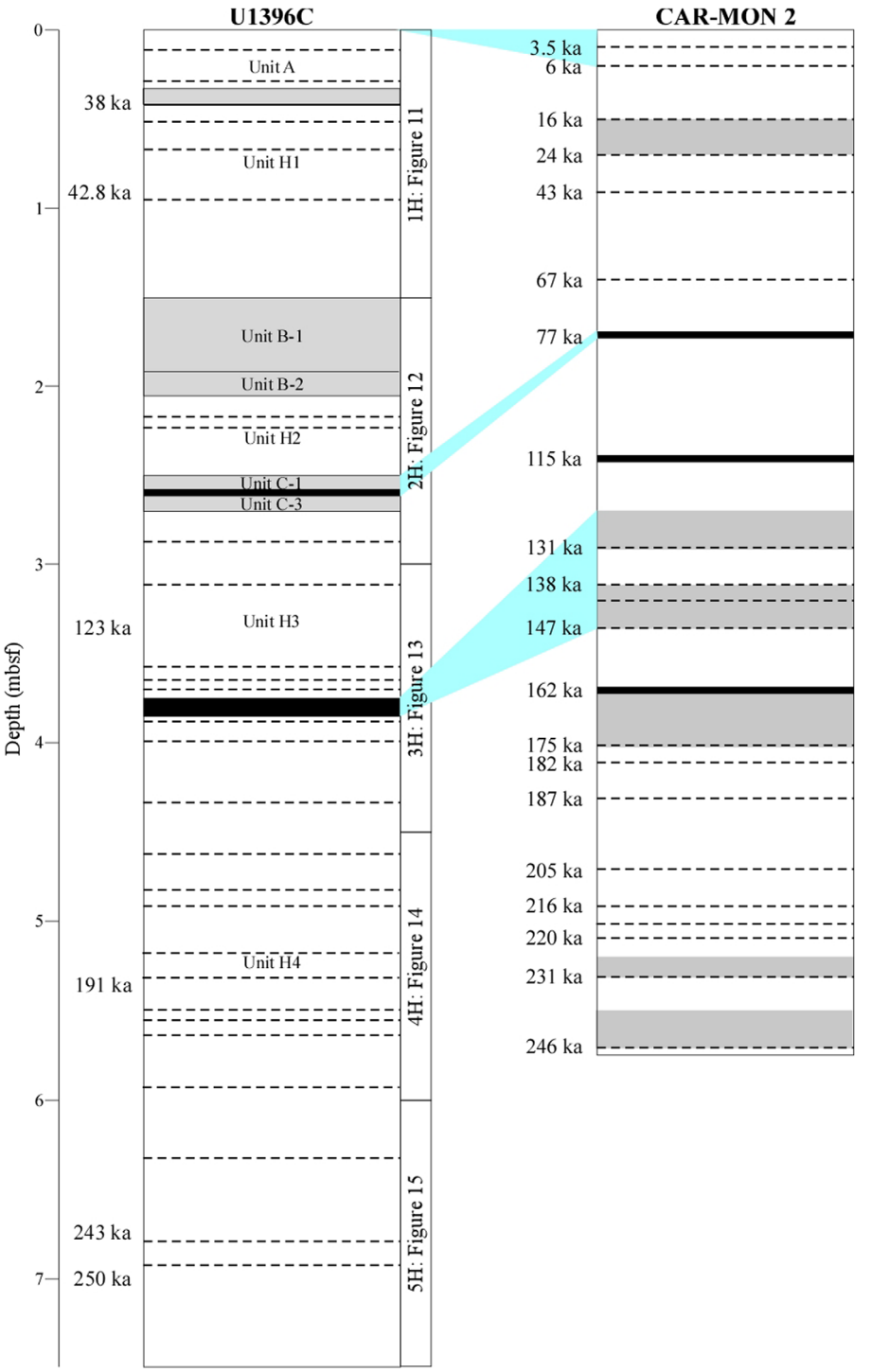

Figure 16. Stratigraphic column for the upper 10 m of U1396C. Geologic units were compiled from shipboard visual core descriptions [*Le Friant et al.*, 2013]. Cryptotephras identified in this study are represented by horizontal black dashed lines. The extent of visible tephra layers (either primary or reworked) are outlined by gray boxes. Thick black solid lines are visible tephras. Ages for U1396C from *Wall-Palmer et al.* [2014]. For comparison, the stratigraphic column of *Le Friant et al.* [2008] for CAR-MON 2 is plotted. Correlations between the two cores are from *Wall-Palmer et al.* [2014].

eruptions in the region with the 29 smaller events representing smaller, more distally sourced, and/or upwind events which considerably expand the initial shipboard-derived tephrochronologic record [*Le Friant et al.*, 2013]. Similar to *Le Friant et al.* [2008], we observe evidence for greater volcanic activity in the earlier

part of the record than the more recent period which possess similar eruptive intervals and repose periods. Notably, we identify an increased period of activity containing five cryptotephra layers between 77 and 131 ka which were previously unrecognized in CAR-MON2 (Figure 16) and was interpreted to reflect a relatively quiet period in the volcanic history of the arc. Only 7.5 m of U1396C has been analyzed; an additional 137 m of material, representing a 4.5 Myr record [*Le Friant et al*., 2013], remains to be investigated. Ongoing work to identify and date both visible tephra and cryptotephra units over the whole core section and to integrate these results with other cores around Montserrat will result in the most complete eruptive record ever produced for the northern Antilles.

5.5. Application to Future Coring Endeavors

Spectroscopic properties and magnetic susceptibility are routinely collected onboard the JOIDES Resolution using the SHMSL. The spectral measurements cover the visible wavelength of light (0.39–0.9 μm), a range that does not include the wavelengths we deemed useful for identification of Fe-rich layers (0.95, 2.2, and 2.35 μm). With restriction to the visible spectrum, SHMSL data collection is potentially missing out on significant opportunities for identification of Fe-rich layers in sediments which could be obtained through collection of the VSWIR spectrum. In addition, collection out to longer wavelengths adds no additional time to the measurement. Data presented here have shown that cryptotephra can be positively identified in a rapid, nondestructive manner using techniques that could be adapted to be completed either shipboard or on land. Integration of these combined data sets can be used to help minimize the need for physical disaggregation of recovered cores. Sediments like those in U1396C are a finite resource, collected at great cost, and must be sampled judiciously in order to meet the needs of the scientific community as well as maintain an archived record for future study. By combining MS, VSWIR, and possibly XRF core scanning methods to identify potential cryptotephra, sampling can be better targeted to those areas that appear to contain cryptotephra and avoid oversampling and destruction of large portions of cored material.

Additionally, although this study demonstrates that VSWIR spectroscopy can be used to identify intermediate to mafic tephra when present in both visible and invisible units within a hemipelagic sediment background, this technique could also be applied to many other geologic settings. As discussed above, many silicates and carbonates have distinguishing features in the VSWIR region of the electromagnetic spectrum allowing identification of the materials present. Therefore, additional spectral indices in this wavelength region could be defined in order to identify materials as disparate as rhyolitic glass, olivine, feldspar, clays, and calcite, from a wide range of geologic environments. The development of identification methods using VSWIR could provide access to diverse samples from varied geologic settings (e.g., marine tephra layers, storm-related sand deposits in peat, and varved sequences) that currently require considerable work to address.

6. Conclusions

We exploited several rapid, complementary, nondestructive techniques for the identification of cryptotephra in marine cores. These methods includes: (1) MS—sensitive to Fe oxides; (2) VSWIR spectroscopy—shown here to be sensitive to Fe-bearing phases in lithics and glasses; (3) XRF core scanning which, although not as rapid a measurement as either MS or VSWIR spectroscopy, is sensitive to several elements in addition to Fe and can be used to help confirm potential cryptotephra identification and/or identify layers not rich in Fe phases. This multi-proxy approach results in a more robust identification of cryptotephra layers as a result of the different chemical properties analyzed by each technique.

This combination of techniques was used to identify 3 visible tephra and 29 potential cryptotephra in IODP core U1396C expanding the current tephrochronological record of the Lesser Antilles arc. Traditional point counting techniques were used to establish a background concentration and then successfully identify regions of increased volcaniclastic deposition (interpreted as cryptotephra) in one of the identified layers in U1396C-1H-1A. This methodology allows for greatly reduced physical sampling of precious drill core material and potentially identification of multiple events within intervals traditionally averaged over during point counting. Combined these methodologies and the development of the new BDI1000VIS spectral parameter are applicable in a host of different environments to distinguish tephra and other Fe-rich layers from background sediment accumulation.

Acknowledgments
The authors acknowledge IODP Expedition 340 for core collection and initial cataloging. The manuscript was greatly improved in revision, thanks to the careful and critical reviews of M. Cassidy and Editor U. Faul. We also thank R. Milliken and K. Robertson for assistance collecting the initial spectral data of the core end-member constituents. We note that there are no data sharing issues since all of the numerical information resulting from the techniques applied in this paper is provided in the figures. This paper was supported by NSF grants EAR-1347868 to M.C.M., EAR-1347912 and OCE-1260671 to R.G.H., and EAR-1347868 to B.J.T.

References

Adams, J. B. (1974), Visible and near-infrared diffuse reflectance spectra of pyroxenes as applied to remote sensing of solid objects in the solar system, *J. Geophys. Res.*, *79*, 4829–4836.

Ananou, B., S. Regnier, Y. Ksari, J. Marfaing, A. Stepanov, Y. Touchard, and P. Rochette (2003), Detection of diluted marine tertiary tephra by electron spin resonance and magnetic measurements, *Geophys. J. Int.*, *155*, 341–349.

Austin, W. E. N., P. M. Abbott, S. M. Davies, N. J. G. Pearce, and S. Wastegård, (2014), Marine tephrochronology: An introduction to tracing time in the ocean, *Geol. Soc. Spec. Publ.*, *398*, 1–5.

Baldridge, A. M., S. J. Hook, C. I. Grove, and G. Rivera (2009), The ASTER spectral library version 2.0., *Remote Sens. Environ.*, *113*, 711–715.

Bibring, J.-P., Y. Langevin, J. F. Mustard, F. Poulet, R. Arvidson, A. Gendrin, B. Gondet, N. Mangold, P. Pinet, and F. Forget (2006), Global mineralogical and aqueous Mars history derived from OMEGA/Mars Express data, *Science*, *312*, 400–404.

Blockley, S. P. E., S. D. F. Pyne-O'Donnell, J. J. Lowe, I. P. Matthews, A. Stone, A. M. Pollard, C. S. M. Turney, and E. G. Molyneux (2005), A new and less destructive laboratory procedure for the physical separation of distal glass tephra shards from sediments, *Quat. Sci. Rev.*, *24*, 1952–1960.

Bonadonna, C., et al. (2002), Tephra fallout in the eruption of Soufrière Hills Volcano, Montserrat, *Geol. Soc. London Mem.*, *21*, 483–516, doi: 10.1144/GSL.MEM.2002.021.01.22.

Brown, F. H., A. M. Sarna-Wojcicki, C. E. Meyer, and B. Haileab (1992), Correlation of Pliocene and Pleistocene tephra layers between the Turkana Basin of East Africa and the Gulf of Aden, *Quat. Int.*, *13–14*, 55–67.

Burns, R. G. (1993), *Mineralogical Applications of Crystal Field Theory*, 2nd ed., 576 pp., Cambridge Top. in Mineral Phys. and Chem., Cambridge Univ. Press, Cambridge, U. K.

Carey, S. N., and H. Sigurdsson (1982), Influence of particle aggregation on deposition of distal tephra from the May 18, 1980, eruption of Mount St. Helens volcano, *J. Geophys. Res.*, *87*, 7061–7072.

Carter, L., and B. Manighetti (2006), Glacial/interglacial control of terrigenous and biogenic fluxes in the deep ocean off a high input, collisional margin: A 139 kyr-record from New Zealand, *Mar. Geol.*, *226*, 307–322.

Carter, L., C. S. Nelson, H. L. Neil, and P. C. Froggatt, (1995), Correlation, dispersal, and preservation of the Kawakawa Tephra and other late Quaternary tephra layers in the Southwest Pacific Ocean, *N. Z. J. Geol. Geophys.*, *38*, 29–46.

Carter, L., B. Alloway, P. Shane, and J. Westgate (2004), Deep-ocean record of major late Cenozoic rhyolitic eruptions from New Zealand, *N. Z. J. Geol. Geophys.*, *47*, 481–500, doi:10.1080/00288306.2004.951507.

Caseldine, C., A. Baker, and W. L. Barnes (1999), A rapid, non-destructive scanning method for detecting distal tephra layers in peats, *Holocene*, *9*, 635–638.

Cassidy, M., R. N. Taylor, M. R. Palmer, R. Cooper, C. Stenlake, and J. Trofimovs, (2012), Tracking the magmatic evolution of an island arc volcano: Insights from a high-precision Pb isotope record of Montserrat, Lesser Antilles, *Geochem. Geophys. Geosyst.*, *13*, Q05003, doi: 10.1029/2012GC004064.

Cassidy, M., S. F. L. Watt, M. R. Palmer, J. Trofimovs, W. Symons, S. E. Maclachlan, and A. J. Stinton (2014a), Construction of volcanic records from marine sediment cores: A review and case study (Montserrat, West Indies), *Earth Sci. Rev., 138*, 137-155.

Cassidy, M., J. Trofimovs, S. F. L. Watt, M. R. Palmer, R. N. Taylor, T. M. Gernon, P. J. Talling, and A. Le Friant (2014b), Multi-stage collapse events in the South Soufrière Hills, Montserrat as recorded in marine sediment cores, in *The Eruption of Soufrière Hills Volcano, Montserrat From 2000 to 2010*, edited by G. Wadge, R. E. A. Robertson, and B. Voight, pp. 381–395, Geol. Soc. of London, London, U. K.

Cloutis, E. A. (2002), Pyroxene reflectance spectra: Minor absorption bands and effects of elemental substitutions, *J. Geophys. Res.*, *107*(E6), doi:10.1029/2001JE001590.

Costa, A., A. Folch, G. Macedonio, B. Giaccio, R. Isaia, and V. C. Smith (2012), Quantifying volcanic ash dispersal and impact of the Campanian Ignimbrite super-eruption, *Geophys. Res. Lett.*, *39*, L10310, doi:10.1029/2012GL051605.

Croudace, I. W., A. Rindby, and R. G. Rothwell (2006), ITRAX: Description and evaluation of a new multi-function x-ray core scanner, in *New Techniques in Sediment Core Analysis*, edited by R. G. Rothwell, pp. 51–63, Geol. Soc. of London, London, U. K.

Davies, S. M., M. Elmquist, J. Bergman, B. Wohlfarth, and D. Hammarlund (2007), Cryptotephra sedimentation processes within two lacustrine sequences from west central Sweden, *Holocene*, *17*, 319–330.

Dearing, J. (1999), *Environmental Magnetic Susceptibility: Using the Bartington MS2 System*, Chi Publishing, Kenilworth, 104 pp. [Available at http://www.gmw.com/magnetic_properties/pdf/Om0409%20J_Dearing_Handbook_iss7.pdf.]

Dugmore, A. (1989), Icelandic volcanic ash in Scotland, *Scot. Geogr. Mag.*, *105*, 168–172.

Eden, D. N., A. S. Palmer, S. J. Cronin, M. Marden, and K. R. Berryman (2001), Dating the culmination of river aggradation at the end of the last glaciation using distal tephra compositions, eastern North Island, New Zealand, *Geomorphology*, *38*, 133–151.

Evans, M. E., and F. Heller (2003), *Environmental Magnetism; Principles and Applications of Enviromagnetics*, Academic, Amsterdam.

Farmer, V. C. (1974), The layer silicates, in *The Infra-Red Spectra of Minerals*, edited by V. C. Farmer, pp. 331–364, The Macaulay Inst. for Soil Res., London, U. K.

Federman, A. N., and S. N. Carey (1980), Electron microprobe correlation of tephra layers from Eastern Mediterranean abyssal sediments and the Island of Santorini, *Quat. Res.*, *13*, 160–171.

Francus P., H. Lamb, T. Nakagawa, M. Marshall, E. Brown, and Suigetsu 2006 Project Members (2009), The potential of high-resolution x-ray fluorescence core scanning: Applications in paleolimnology, *PAGES News*, *17*, 93–95.

Gehrels, M. J., R. M. Newnham, D. J. Lowe, S. Wynne, Z. J. Hazell, and C. Caseldine (2008), Towards rapid assay of cryptotephra in peat cores: Review and evaluation of various methods, *Quat. Int.*, *178*, 68–84.

Grönvold, K., N. Óskarsson, S. J. Johnsen, H. B. Clausen, C. U. Hammer, G. Bond, and E. Bard (1995), Ash layers from Iceland in the Greenland GRIP ice core correlated with oceanic and land sediments, *Earth Planet. Sci. Lett.*, *135*, 149–155.

Grousset, F. E., L. Labeyrie, J. A. Sinko, M. Cremer, G. Bond, J. Duprat, E. Cortijo, and S. Huon (1993), Patterns of ice-rafted detritus in the glacial North Atlantic (40–55°N), *Paleoceanography*, *8*, 175–192.

Gunn, D. E., and A. I. Best (1998), A new automated nondestructive system for high resolution multi-sensor core logging of open sediment cores, *Geo Mar. Lett.*, *18*, 70–77.

Harford, C. L., M. S. Pringle, R. S. J. Sparks, and S. R. Young (2002), The volcanic evolution of Montserrat using $^{40}Ar/^{39}Ar$ geochronology, in *The Eruption of Soufrière Hills Volcano, Montserrat, From 1995 to 1999*, edited by T. H. Druitt and B. P. Kokelaar, pp. 93–113, Geol. Soc., London, U. K.

Hecker, C., S. Hook, M. van der Meijde, W. Bakker, H. van der Werff, H. Wilbrink, F. van Ruitenbeek, B. de Smeth, and F. van der Meer (2011), Thermal infrared spectrometer for earth science remote sensing applications—Instrument modifications and measurement procedures, *Sensors*, *11*, 10,981–10,999.

Hook, S. J., E. A. Abbott, C. Grove, A. B. Kahle, and F. Palluconi (1999), The use of multispectral thermal infrared data in geologic studies, in *Manual of Remote Sensing*, 3rd ed., edited by A. N. Rencz and R. A. Ryerson, pp. 59–110, John Wiley, N. Y.
Hooper, D. M., and D. M. Necsoiu (2011), Spectroscopic analysis of tephra as a site characterization tool, in *U.S. Nuclear Regulatory Commission Contract NRC–02–07–006*, pp. 1–21, Cent. for Nucl. Waste Regul. Anal., San Antonio, Tex.
Houghton, B. F., C. J. N. Wilson, and D. M. Pyle (2000), Pyroclastic fall deposits, in *Encyclopedia of Volcanoes*, edited by H. Sigurdsson, pp. 555–570, Academic, San Diego, Calif.
Jansen, J. H. F., S. J. Van der Gaast, B. Koster, and A. J. Vaars (1998), CORTEX, a shipboard XRF-scanner for element analyses in split sediment cores, *Mar. Geol.*, *151*, 143–153.
Jutzeler, M., J. D. L. White, P. J. Talling, M. C. McCanta, and S. Morgan (2014), Identification of coring disturbances in IODP piston cores and implications for offshore record of volcanic events and the Missoula mega-floods, *Geochem. Geophys. Geosyst.*, *15*, 3572–3590, doi:10.1002/2014GC005447.
Keppler, H. (1992), Crystal field spectra and geochemistry of transition metal ions in silicate melts and glasses, *Am. Mineral.*, *77*, 62–75.
King, T. V. V., and I. W. Ridley (1987), Relation of the spectroscopic reflectance of olivine to mineral chemistry and some remote sensing implications, *J. Geophys. Res.*, *92*, 11,457–11,469.
Knudsen, K. L., and J. Eiríksson (2002), Application of tephrochronology to the timing and correlation of palaeoceanographic events recorded in Holocene and Late Glacial shelf sediments off North Iceland, *Mar. Geol.*, *191*, 165–188.
Kristjánsdóttir, G. B., J. S. Stoner, A. E. Jennings, J. T. Andrews, and K. Grönvold (2007), Geochemistry of Holocene cryptotephras from the North Iceland Shelf (MD99-2269): Intercalibration with radiocarbon and palaeomagnetic chronostratigraphies, *Holocene*, *17*, 155–176.
Kristjansson, L., and G. Jonsson (2007), Paleomagnetism and magnetic anomalies in Iceland, *J. Geodyn.*, *43*, 30–54.
Kylander, M. E., E. M. Lind, S. Wastegård, and L. Löwemark (2012), Recommendations for using XRF core scanning as a tool in tephrochronology, *Holocene*, *22*, 371–375.
Labanieh, S., C. Chauvel, A. Germa, X. Quidelleur, and E. Lewin (2010), Isotopic hyperbolas constrain sources and processes under the Lesser Antilles arc, *Earth Planet. Sci. Lett.*, *298*, 35–46, doi:10.1016/j.epsl.2010.07.018.
Langdon, P. G., C. J. Caseldine, I. W. Croudace, S. Jarvis, S. Wastegård, and T. C. Crowford (2011), A chronomid-based reconstruction of summer temperatures in NW Iceland since AD 1650, *Quat. Res.*, *75*, 451–460.
Larsen, G. (2010), Katla: Tephrochronology and eruption history, *Dev. Quat. Sci.*, *13*, 23–49.
Larsen, G., and J. Eiríksson (2007), Late Quaternary terrestrial tephrochronology of Iceland—Frequency of explosive eruptions, type and volume of tephra deposits, *J. Quat. Sci.*, *23*, 109–120.
Larsen, G., J. Eiriksson, K. L. Knudsen, and J. Heinemeier (2002), Correlation of late Holocene terrestrial and marine tephra markers, north Iceland: Implications for reservoir age changes, *Polar Res.*, *21*, 283–290.
Le Friant, A., E. J. Lock, M. B. Hart, G. Boudon, R. S. J. Sparks, M. J. Leng, C. W. Smart, J. C. Komorowski, C. Deplus, and J. K. Fisher (2008), Late Pleistocene tephrochronology of marine sediments adjacent to Montserrat, Lesser Antilles volcanic arc, *J. Geol. Soc.*, *165*, 279–290, doi:10.1144/0016-76492007-019.
Le Friant, A., O. Ishizuka, N. A. Stroncik, and Expedition 340 Scientists (2013), Lesser Antilles Volcanism and landslides: Implications for hazard assessment and long-term magmatic evolution of the arc, Proc. Integrated Ocean Drill. Program, *340*, doi:10.2204/iodp.pr.340.2013.
Lindsay, J. M., R. B. Trumbull, and W. Siebel (2005), Geochemistry and petrogenesis of late Pleistocene to recent volcanism in Southern Dominica, Lesser Antilles, *J. Volcanol. Geotherm. Res.*, *148*, 253–294, doi:10.1016/j.jvolgeores.2005.04.018.
Lowe, D. J. (2011), Tephrochronology and its application: A review, *Quat. Geochron.*, *6*, 107–153, doi:10.1016/j.quageo.2010.08.003.
Lowe, D. J. (2014), Marine tephrochronology: A personal perspective, *Geol. Soc. Spec. Publ.*, *398*, 7–19.
Lowe, D. J., and J. B. Hunt (2001), A summary of terminology used in tephra-related studies, in *Tephras: Chronology, Archaeology*, vol.1, edited by E. T. Juvigne and J.-P. Raynal, pp. 17–22, CDERAD Editeur, Goudet, France.
Lucey, P. G., G. J. Taylor, and E. Malaret (1995), Abundance and distribution of iron on the Moon, *Science*, *268*, 1150–1153.
Matthews, N. E., V. C. Smith, A. Costa, A. J. Durant, D. M. Pyle, and N. J. G. Pearce (2012), Ultra-distal tephra deposits from super-eruptions: Examples from Toba, Indonesia and Taupo Volcanic Zone, New Zealand, *Quat. Int.*, *258*, 54–79.
Moreno, A., S. Giralt, B. Valero-Garcés, A. Sáez, R. Bao, R. Pregoe, J. J. Pueyo, P. González-Sampériz, and C. Taberner (2007), A 14 kyr record of the tropical Andes: The Lago Chungará sequence (18°S, northern Chilean Altiplano), *Quat. Int.*, *161*, 4–21.
Murchie, S., L. Kirkland, S. Erard, J. Mustard, and M. Robinson (2000), Near-infrared spectral variations of Martian surface materials from ISM imaging spectrometer data, *Icarus*, *147*, 444–471.
Mustard, J. F., et al. (2008), Hydrated silicate minerals on Mars observed by the Mars Reconnaissance Orbiter CRISM instrument, *Nature*, *454*, 305–309.
Naranjo, J. A., F. Henríquez, and J. O. Nyström (2010), Subvolcanic contact metasomatism at El Laco Volcanic Complex, Central Andes, *Andean Geol.*, *1*, 110–120.
Ninkovich, D., R. S. J. Sparks, and M. T. Ledbetter (1978), The exceptional magnitude and intensity of the Toba eruption, Sumatra: An example of the use of deep-sea tephra layers as a geological tool, *Bull. Volcanol.*, *41*, 286–298.
Ólafsdóttir, S., A. Geirsdóttir, G. H. Miller, J. S. Stoner, and J. E. T. Channell (2013), Synchronizing Holocene lacustrine and marine sediment records using paleomagnetic secular variation, *Geology 41*, 535–538, doi:10.1130/G33946.1.
Pälike, H., M. Lyle, H. Nishi, I. Raffi, K. Gamage, A. Klaus, and the Expedition 320/321 Scientists (2010), Expedition 320/321 summary, Proc. Integrated Ocean Drill. Program, 320/321, doi:10.2204/iodp.proc.320321.2010.
Payne, R., J. Blackford, and J. van der Plicht (2008), Using cryptotephras to extend regional tephrochronologies: An example from southeast Alaska and implications for hazard assessment, *Quat. Res.*, *69*, 42–55.
Pelkey, S. M., et al. (2007), CRISM multispectral summary products: Parameterizing mineral diversity on Mars from reflectance, *J. Geophys. Res.*, *112*, E08S14, doi:10.1029/2006JE002831.
Peters, C., W. E. N. Austin, J. Walden, and F. D. Hibbert (2010), Magnetic characterisation and correlation of a Younger Dryas tephra in North Atlantic marine sediments, *J. Quat. Sci.*, *25*, 339–347.
Pieters, C. M., and P. A. J. Englert (1993), *Remote Geochemical Analysis: Elemental and Mineralogical Composition*, 594 pp., Cambridge Univ. Press, Cambridge, U. K.
Polgreen, E. L., W. W. Sager, F. R. Rack, and R. J. van Waasbergen (1993), Magnetic properties of Pliocene–Pleistocene sediments from Hole 810C, Shatsky Rise, and implications for the origin and correlatability of their magnetic susceptibility variations, in *Proceedings of Ocean Drill. Program, Scientific Results*, vol. 132, edited by J. H. Natland et al., pp. 37–45, Ocean Drill. Program, College Station, Tex., doi:10.2973/odp.proc.sr.132.303.1993.
Rasmussen, T. L., S. Wastegård, A. Kuijpers, T. C. E. van Weering, J. Heinemeier, and E. Thomsen (2003), Stratigraphy and distribution of tephra layers in marine sediment cores from the Faeroe Islands, North Atlantic, *Mar. Geol.*, *199*, 263–277.

Reid, R. P., S. N. Carey, and D. R. Ross (1996), Late Quaternary sedimentation in the Lesser Antilles island arc, *Geol. Soc. Am. Bull.*, *108*, 78–100, doi:10.1130/0016-7606(1996)108 < 0078:LQSITL>2.3.CO;2.
Rivkin, A. S., and J. P. Emery (2010), Detection of ice and organics on an asteroidal surface, *Nature*, *464*, 1322–1323.
Roberts, A. P., B. Lehman, R. J. Weeks, K. L. Verosub, and C. Laj (1997), Relative paleointensity of the geomagnetic field over the last 200,000 years from ODP Sites 883 and 884, North Pacific Ocean, *Earth Planet. Sci. Lett.*, *152*, 11–23.
Robinson, S. G. (1986), The late Pleistocene paleoclimatic record of North Atlantic deep-sea sediments revealed by mineral-magnetic measurements, *Phys. Earth Planet. Inter.*, *42*, 22–47.
Rose, W. I., and C. A. Chesner (1987), Dispersal of ash in the great Toba eruption, 75 ka, *Geology*, *15*, 913.
Salisbury, J. W., L. S. Walter, N. Vergo, and D. M. D'Aria (1991), *Infrared (2.1–25 μm) Spectra of Minerals*, 267 pp., Johns Hopkins Univ. Press, Baltimore, Md.
Shane, P. (2000), Tephrochronology: A New Zealand case study, *Earth Sci. Rev.*, *49*, 223–259.
Shane, P., and I. C. Wright (2011), Late Quaternary tephra layers around Raoul and Macauley Islands, Kermadec Arc: Implications for volcanic sources, explosive volcanism and tephrochronology, *J. Quat. Sci.*, *26*, 422–432, doi:10.1002/jqs.1468.
Shane, P., M. Gehrels, A. Zawalna-Geer, P. Augustinus, J. Lindsay, and I. Chaillou (2013), Longevity of a small shield volcano revealed by crypto-tephra studies (Rangitoto volcano, New Zealand): Change in eruptive behavior of a basaltic field, *J. Volcanol. Geotherm. Res.*, *257*, 174–183.
Smith, W. H. F., and D. T. Sandwell (1997), Global seafloor topography from satellite altimetry and ship depth soundings, *Science*, *277*, 1957–1962.
Spinetti, C., F. Mazzarini, R. Casacchia, L. Colini, M. Neri, B. Behncke, R. Salvatori, M. F. Buongiorno, and M. T. Pareschi (2009), Spectral properties of volcanic materials from hyperspectral field and satellite data compared with LiDAR data at Mt. Etna, *Int. J. Appl. Earth Obs. Geoinf.*, *11*, 142–155.
Stinton, A. J., P. D. Cole, H. M. Odbert, T. Christopher, G. Avard, and M. Bernstein (2014), Dome growth and valley fill during Phase 5 (8 October 2009 – 11 February 2010) at the Soufrière Hills Volcano, Montserrat, in *The Eruption of Soufrière Hills Volcano, Montserrat, From 2000 to 2010, Geol. Soc. London Mem. 39*, edited by G. Wadge, R. E. A. Robertson, and B. Voight, pp. 113–131, Geol. Soc. of London, London, U. K.
Stoner, J. S., and J. T. Andrews (1999), The North Atlantic as a Quaternary magnetic archive, in *Quaternary Climates, Environments and Magnetism*, edited by B. A. Maher and R. Thompson, pp. 49–80, Cambridge Univ. Press, Cambridge, U. K.
Stoner, J. S., J. E. T. Channell, and C. Hillaire-Marcel (1996), The magnetic signature of rapidly deposited detrital layers from the deep Labrador Sea: Relationship to North Atlantic Heinrich layers, *Paleoceanography*, *11*, 309–325.
Stoner, J. S., A. Jennings, G. B. Kristjánsdóttir, G. Dunhill, J. T. Andrews, and J. Hardardóttir (2007), A paleomagnetic approach toward refining Holocene radiocarbon-based chronologies: Paleoceanographic records from the north Iceland (MD99-2269) and east Greenland (MD99-2322) margins, *Paleoceanography*, *22*, PA1209, doi:10.1029/2006PA001285.
Svensson, A., K. K. Andersen, M. Bigler, H. B. Clausen, D. Dahl-Jensen, S. M. Davies, S. J. Johnsen, R. Muscheler, S. O. Rasmussen, and R. Röthlisberger (2006), The Greenland Ice core chronology 2005, 15–42ka. Part 2: Comparison to other records, *Quat. Sci. Rev.*, *25*, 3258–3267.
Thomas, R. G., Y. Guyodo, and J. E. T. Channell (2003), U channel track for susceptibility measurements, *Geochem. Geophys. Geosyst.*, *4*(6), 1050, doi:10.1029/2002GC000454.
Thompson, R., and F. Oldfield (1986), *Environmental Magnetism*, 227 pp., Allen and Unwin, London, U. K.
Thompson, R., R. W. Battarbee, P. E. O'Sullivan, and F. Oldfield (1975), Magnetic susceptibility of lake sediments, *Limnol. Oceanogr.*, *20*, 687–698.
Tirsch, D., R. A. Craddock, T. Platz, A. Maturilli, J. Helbert, and R. Jaumann (2012), Spectral and petrologic analyses of basaltic sands in Ka'u Desert (Hawaii)—Implications for the dark dunes on Mars, *Earth Surf. Processes Landforms*, *37*, 434–448, doi:10.1002/esp.2266.
Trofimovs, J., et al. (2006), Submarine pyroclastic deposits formed at the Soufrière Hills Volcano, Montserrat (1995-2003): What happens when pyroclastic flows enter the ocean?, *Geology*, *34*, 549–552, doi:10.1130/G22424.1.
Trofimovs, J., R. S. J. Sparks, and P. J. Talling (2008), Anatomy of a submarine pyroclastic flow and associated turbidity current: July 2003 dome collapse, Soufrière Hills volcano, Montserrat, West Indies, *Sedimentology*, *55*, 617–634.
Trofimovs, J., et al. (2013), Timing, origin, and emplacement dynamics of mass flows offshore of SE Montserrat in the last 110 ka: Implications for landslide and tsunami hazards, eruption history and volcanic island evolution, *Geochem. Geophys. Geosyst.*, *14*, 385–406, doi:10.1002/ggge.20052.
Turney, C. S. M. (1998), Extraction of rhyolitic component of Vedde microtephra from minerogenic lake sediments, *J. Paleolimnol.*, *19*, 199–206.
Turney, C. S. M., and J. J. Lowe (2001), Tephrochronology, in *Tracking Environmental Changes in Lake Sediments: Physical and Chemical Techniques*, edited by W. M. Last and J. P. Smol, pp. 451–471, Kluwer Acad., Dordrecht, Netherlands.
van den Bogaard, C., and H.–U. Schmincke (2002), Linking the North Atlantic to central Europe: A high-resolution Holocene tephrochronological record from northern Germany, *J. Quat. Sci.*, *17*, 3–20, doi:10.1002/jqs.636.
van den Bogaard, C., W. Dörfler, P. Sandgren, and H.–U. Schmincke (1994), Correlating the holocene records: Icelandic tephra found in Schleswig-Holstein (Northern Germany), *Naturwissenschaften*, *81*, 554–556.
Wall-Palmer, D., M. B. Hart, C. W. Smart, R. S. J. Sparks, A. Le Friant, G. Boudon, C. Deplus, and J. C. Komorowski (2012), Pteropods from the Caribbean Sea: Variations in calcification as an indicator of past ocean carbonate saturation, *Biogeosciences*, *9*, 309–315.
Wall-Palmer, D., et al. (2014), Late Pleistocene stratigraphy of IODP Site U1396 and compiled chronology offshore of south and south west Montserrat, Lesser Antilles, *Geochem. Geophys. Geosyst.*, *15*, 3000–3020, doi:10.1002/2014GC005402.
Watt, S. F. L., et al. (2012), Widespread and progressive seafloor-sediment failure following volcanic debris avalanche emplacement: Landslide dynamics and timing offshore Montserrat, Lesser Antilles, *Mar. Geol.*, *323-325*, 69–94, doi:10.1016/j.margeo.2012.08.002.

Erratum

In the originally published version of this article, there was an omission in the acknowledgments section. The text has since been updated and this version may be considered the authoritative version of record.